Nanoengineered Surfaces for Advanced Thermal Management

by

Rong Xiao

SUBMITTED TO THE DEPARTMENT OF MECHANICAL ENGINEERING IN
PARTIAL FULFILLMENT OF THE REQUIREMENTS FOR THE DEGREE OF

MASTER OF SCIENCE IN MECHANICAL ENGINEERING
AT THE
MASSACHUSETTS INSTITUTE OF TECHNOLOGY

JUNE 2009

Signature of Author:
Department of Mechanical Engineering
May 29, 2009

Certified by:
Evelyn N. Wang
Assistant Professor of Mechanical Engineering
Thesis Supervisor

Accepted by:
David Hardt
Professor of Mechanical Engineering
Chairman, Graduate Thesis Committee

Nanoengineered Surfaces for Advanced Thermal Management
By

Rong Xiao

Submitted to the Department of Mechanical Engineering
On May 29, 2008 in partial fulfillment of the
Requirements for the Degree of Master of Science in
Mechanical Engineering

Abstract

Thermal management is a critical challenge for a variety of applications including integrated circuits (ICs) and energy conversion devices. As the heat fluxes exceed 100 W/cm^2, novel cooling solutions need to be developed. Thin film evaporation is a promising approach because the large latent heat associated with phase change can be utilized while the thermal resistance associated with the liquid film thickness can be minimized. However, traditional thin film evaporation schemes such as jet impingement and sprays suffer from several limitations, such as high power consumption, complex flow patterns, and localized cooling

In this thesis, micro- and nanostructured surfaces were investigated to enhance fluid and heat transport for thin film evaporation. This thesis includes studies of fluid interactions on surfaces with micro- and nanopillar arrays with diameters and spacings ranging from 500 nm to 10 μm. First, liquid transport studies were performed where a propagating liquid on an array of pillars with scalloped features can separate into multiple layers of liquid films. The scallops were found to act as energy barriers that favored liquid separation into several layers. An analytical model based on surface energy was developed to explain the phenomenon and was validated by experiments on additional tailored pillar geometries. Subsequently, a semi-analytical model was developed to predict the propagation velocity based on Modified Washburn's Model to optimize propagation of the liquid. The results were validated by measurements of liquid propagation velocity on micropillar arrays with various geometries. Finally, the heat transfer performance was investigated on microstructure pillar arrays with integrated heaters and temperature sensors. These test devices were fabricated and the behavior of the thin liquid film under varying heat fluxes was investigated, where a two-step "dry-out" behavior was observed. The thermal resistance of the thin film including the effect of the micropillars was also analyzed. This work demonstrates the potential of micro- and nanostructures to achieve high heat fluxes *via* thin film evaporation.

Thesis Supervisor: Evelyn N. Wang
Title: Assistant Professor of Mechanical Engineering

Contents

Chapter 1: Background

Micro-Electro-Mechanical Systems

Micro-Electro-Mechanical Systems (MEMS) is a field that integrates mechanical elements, sensors, actuators and electronics on the order of microns and nanometers through microfabrication techniques. At these scales, the surface to volume ratio becomes large such that surface effects such as capillarity and adhesion dominate over volume effects such as gravity or inertia. These advantages provide opportunities to create miniaturized devices with favorable features such as low power consumption and fast dynamic response.

The potential of MEMS technology was predicted in Richard Feynman's famous talk *There's Plenty of Room at the Bottom* in 1959 [1]. After fifty years of development, the MEMS industry has experienced significant growth with the advent of commercially available MEMS devices used in our daily lives, including micromirror arrays in projectors, implantable medical devices, microantennas in cell phones, and microaccelerometers in gaming consoles [2].

Microfluidics

One active sub-area of MEMS is microfluidics, *e.g.*, where liquids flow in microchannels or on surfaces with microstructures. The length scale of such systems ranges a few to several hundred microns, which is significantly smaller than the capillary length, *e.g.*, 2.7 mm for water. Dimensionless groups such as the Weber number, which compares inertia force to surface tension, the Capillary number, which compares viscous force to surface tension, and the Bond number, which compares gravity to surface tension, are all typically small. This regime offers new dominant physics compared to the macroscale, particularly related to surface tension, which offers exciting new opportunities and complexities. An area of significant interest in microfluidics research is for the development of thermal management solutions.

Thermal Management Needs

Thermal Management for High Performance Integrated Circuits

The continual demand for increased processing performance and reduced size of modern microprocessors has introduced new challenges in thermal management. The necessary heat dissipation rate of the original Pentium CPU in 1990s was around 30 W/cm^2 and was achieved by forced air cooling. With the development of the Pentium Dual-Core released in 2007, forced air flow combined with heat pipes were used to dissipate heat flux of approximately 70 W/cm^2 [3]. The International Technology Roadmap for Semiconductors (ITRS) projects that the power density for the 14 nm generation chips will be higher than 100 W/cm^2 by 2015 [4]. A more aggressive outlook for IC chips was proposed by Thome where chips may require over 300 W/cm^2 of power removal in the next few years [5]. Shankar *et al.* estimated power densities to be an order of magnitude higher than the projected values by ITRS, which is as high as 1000 W/cm^2 [6]. Fig.1-1 shows the demand of electronics cooling in comparison with other thermal systems. We can see that the heat fluxes of integrated circuit chips are on the same order of magnitude as a rocket nozzle throat while the allowed working temperature is much lower, which requires the thermal resistance to be ultra low.

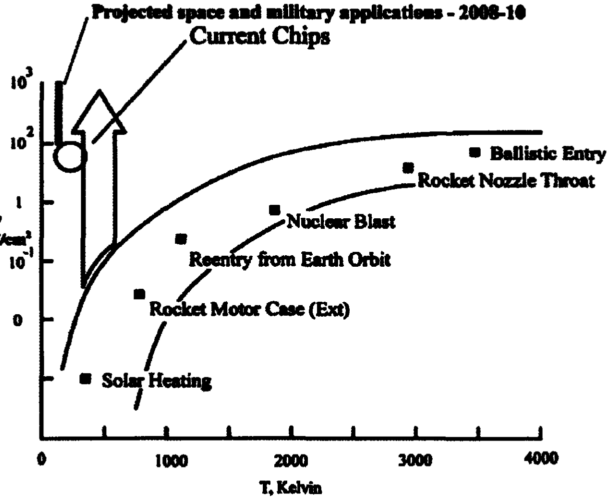

Fig. 1-1 Comparison of projected thermal management demands for various thermal systems by Oktay *et al.* and re-drawn by Kandlikar *et al.* [7]

The need for advanced thermal management strategies which are capable of dissipating heat fluxes of 10^2-10^3 W/cm^2 with a low temperature rise has been well recognized by the electronics industry. In addition, the popular trend of smaller volume of consumer electronics requires the thermal management system to be compact, which poses another challenge.

Thermal Management for Energy Systems

In addition to the microprocessor industry, thermal management is important for a broad range of areas, especially in systems involving energy conversion. One example is solar cells where the energy conversion efficiency is sensitive to temperature. For most crystalline solar cells, the efficiency decreases 0.5% when temperature increases by one degree Celsius [8]. Without effective thermal management methods, efforts to increase conversion efficiency can be offset by the rise in temperature. Similar thermal management challenges are faced in high temperature solid oxide fuel cells [9].

Current Cooling Schemes and Challenges

From the above discussion, thermal management is an important aspect in various systems, and there has been significant effort devoted to the development of effective and innovative heat dissipation schemes. Methods for heat removal include natural convection, single-phase forced convection, and boiling. Heat transfer coefficients have been presented by Mudawar [14] with a few of these cooling mechanisms shown in Fig.1-2.

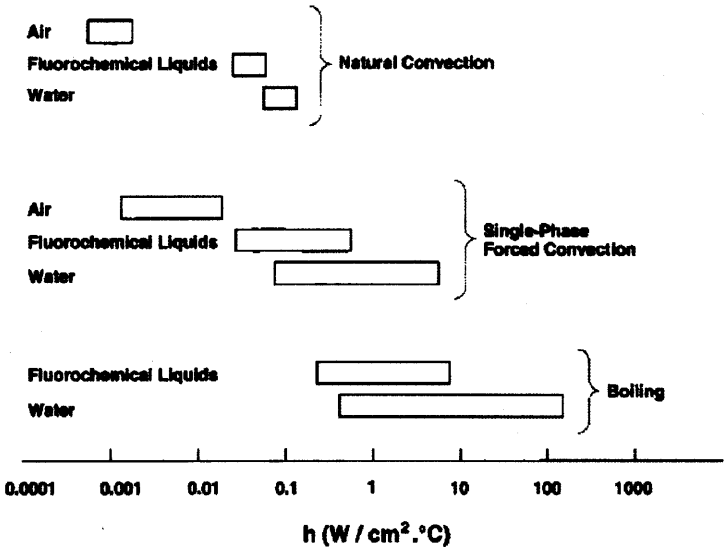

Fig. 1-2 Comparison of heat transfer coefficients (*h*) attainable with various heat removal mechanisms using various liquids [10].

To achieve desired high heat fluxes of several hundreds of Watts per square centimeter with a reasonable temperature rise, phase change (boiling), which utilizes the large latent heat of vaporization, is one of the practical mechanisms. There are several different phase change cooling approaches, including pooling boiling, flow boiling, jet impingement and spray. Their advantages and challenges will be emphasized below.

Pool boiling is considered one of the simplest methods to achieve heat fluxes over 100 W/cm^2. Pooling boiling is a passive method which doesn't require extra power input. However, the maximum heat transfer rate of pool boiling is limited by the critical heat flux (CHF), above which the transition from nucleate boiling to film boiling occurs and there is a significant rise in thermal resistance and superheat. According to Zuber's model, which accounts for the hydrodynamic stability of the vapor escape column, the CHF of dielectric liquids commonly used for electronics cooling, such as FC-72 and FC-78, are relatively low (around 20 W/cm^2) on flat surfaces. With saturated water at 1 atm on a flat surface, the CHF can be enhanced to around 110 W/cm^2, and is well-supported by experiments [11]. Various models on the CHF limit have been proposed, such as Dhir and Liew's model based on capillary pumping [12] and Liter and Kaviany's model on viscous drag [13]. Extensive work has focused on enhancing the CHF limit. Surfaces have been modified by creating microstructures such as cavities and studs or by depositing porous layers or nanoparticles. Kim *et al.* suggested a fourfold enhancement of CHF is possible with the contact angle reduced from 70^o to 20^o [14]. You *et al.* reported a 200% increase of CHF in nanofluids containing 0.005 g/l of alumina nanoparticles [15]. More recently, nanowire and nanotube forests have also demonstrated the ability to double the CHF with water on silicon surfaces [16]. While the detailed mechanism for surface modifications to enhance CHF is still under investigation and debate, the general consensus is that the cavities within the microstructures act as nucleation sites and the increased surface roughness enhances liquid pumping to avoid drying out.

Flow boiling in channels has demonstrated promising potential for high flux cooling. Due to the large surface to volume ratio, flow boiling in microchannels, where thermal resistance below 0.1W/K has been achieved, has been shown to be advantageous over its macroscale counterpart. However, microchannel boiling suffers from several challenges and hurdles. The pressure drop across the microchannels can be as high as 1 atm [7] due to the large friction, which requires high power pumping system to drive the flow and lowers the overall efficiency. In macrochannels, vapor bubbles are removed by inertia and buoyancy forces, which are insignificant at the microscale. As a result, the vapor bubbles tend to remain in the channel and expand to vapor slugs very rapidly, which lead to local dry-outs, non-uniform distribution and flow instabilities or even flow reversal. With constrictors at the entrance of the channel to stabilize the flow, Kosar *et al.* achieved heat flux as high as 614 W/cm^2 by water flow boiling in microchannels [17]. However, such constrictors further increase the pressure drop and the energy consumption.

In jet impingement cooling system, high-velocity jets from nozzles impinge on the hot surface and form a very thin liquid layer under the jet. Previous work showed that the jet velocity and sub-cooling of the liquid have a pronounced effect on the heat flux [10]. Wang *et al.* achieved heat fluxes of 90 W/cm^2 with a temperature rise of 100 ^oC [18]. However, jet impingement schemes are difficult to implement, where only the local impingement region experiences high heat removal rates, and the flooding of the chambers lead to pool boiling which limits the cooling performance. Similar to jet impingement, spray cooling utilizes liquid droplets to impinge on the hot surface and form a very thin liquid layer. The evaporation of the thin layer removes a large amount of heat. Lin and Ponnappan reported a maximum heat flux of 500 W/cm^2 with water spray from eight nozzles [19]. However, ultra high pressure (hundreds of kPa) is required to create spray flow, which can hardly be allowed in commercial packages. Researchers have also proposed using piezoelectric vibrators or inkjet printer technology to create sprays [20]. Recently, growing interest has focused on surface modification to enhance the heat removal [21-23]. In addition to the ultra high pressure and power needed, another concern about spray cooling is the intricate flow patterns. Hall and Mudawar reported that identical spray nozzles from the same production batch failed to create identical spray flows [24].

Thin Film Evaporation

As stated above, the high heat flux in jet impingement and spray cooling all result from evaporation of the thin liquid layer. Fig.1-3(a) shows a schematic of thin film evaporation for heat dissipation. The thermal resistance at the liquid-vapor interface is negligible due to the phase-change process at the interface. As a result, the thermal resistance is almost completely due to the conduction within the liquid film, which is determined by

$$R = h / k \tag{1-1}$$

where R is the thermal resistance, h is the thickness of the liquid film and k is the thermal conductivity of the liquid. The relationship between the thermal resistance and the film thickness for water is shown in Fig.1-3(b).

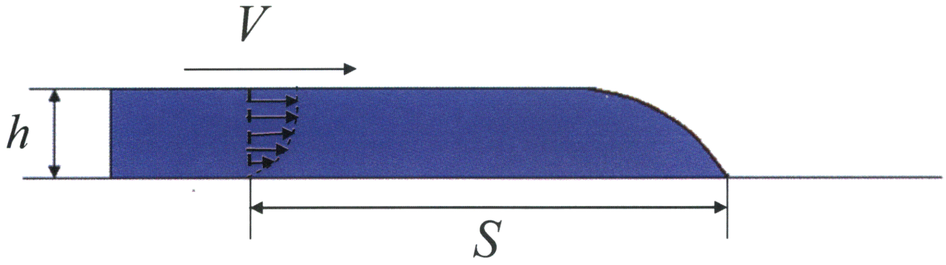

(a)

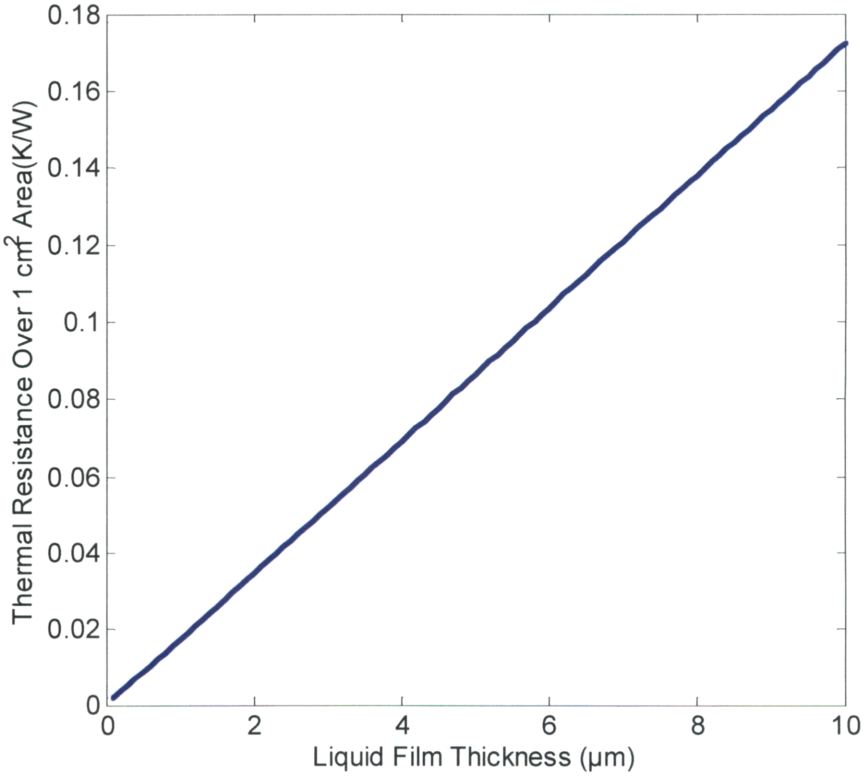

(b)

Fig. 1-3 (a) Schematic showing the concept of thin film evaporation for heat dissipation. (b) The thermal resistance of the liquid film as a function of film thickness for water. To achieve thermal resistance below 0.1 K/(W· cm^2), the thickness of the film needs to be below 6 μm.

According to energy conservation, the heat removal rate can be determined by:

$$q'' = h_{fg}\rho V h / S \tag{1-2}$$

where h_{fg} is the latent heat of the liquid, ρ is the density of the liquid, V is the propagation velocity of the liquid, h is the thickness of the liquid film, S is the area of the liquid film.

However, based on the discussions above, traditional jet impingement and sprays are limited in performance and cannot achieve thin film evaporation due to various limitations. Researchers have investigated alternative schemes. For example, Qi *et al.* proposed to use electrohydrodynamic (EHD)-enhanced polarization pump to deliver and maintain an ultra-thin liquid film. Their experiments demonstrated the heat removal rate of 20-40 W/cm^2 with significant lower temperature rise than spray cooling and pool boiling [25]. However, their method requires very strong electrical field to drive the liquid film, which limits its implementation. In this work, we investigated the potential of micro- and nanostructures to help form and control the thin liquid film to overcome the existing challenges with jet impingement and spray cooling methods. In Chapter 2, we focus on a phenomenon where defined nanostructure geometries cause the liquid to separate into multiple layers with varying thicknesses during the spreading process. This phenomenon is of interest because it offers opportunities to control the liquid film thickness, hence minimizing the thermal resistance of the liquid film. In Chapter 3, the planar propagation rate driven by capillarity in pillars array was studied. A semi-analytical model to predict the propagation rate was derived and validated by experiments. In Chapter 4, we performed experiments on thin film evaporation using microstructured surfaces. We integrated heaters and sensors on the back side of the devices to emulate both uniform and non-uniform heat fluxes on integrated chips and to simultaneously measure the temperature distribution. In Chapter 5, conclusions and future work are discussed.

Chapter 2: Multi-layer Spreading

Wetting Phenomena and Structured Surfaces

To create a thin liquid film, the utilization of micro- or nanostructures on the surface is a promising approach. However, a fundamental understanding of the wetting phenomena, which involves rich and complex interactions between the liquid and solid, is critical. Wenzel in 1936 first proposed that the surface roughness can magnify the hydrophobicity and the hydrophilicity of the material, which is called the Wenzel Model [26] (When the contact angle of water on a solid surface is smaller than 90 degrees, the surface is termed hydrophilic, otherwise, it is termed hydrophobic). Later, Cassie and Baxter discovered another configuration where air is trapped within the surface roughness features and the liquid rests on such a composite surface, yielding a superhydrophobic surface with even a higher apparent contact angle than in the Wenzel state [27]. With the development of microfabrication techniques, superhydrophobic (when the contact angle is larger than 160 degrees) or superhydrophilic (when the contact angle is almost zero degrees) surfaces with well-controlled micro- or nanofeatures have been realized. A significant body of work has focused on the design, analysis, and fabrication of superhydrophobic surfaces which demonstrated great potential in self-cleaning and drag-reduction [28-32]. With delicate nanofeatures, oleophobic or omni-phobic surfaces, which display contact angle higher than 150 degrees with even low surface tension liquid, have been achieved [33-34]. Recently, there has been more attention on superhydrophilic surfaces where liquids can form thin layers on such surfaces. The ability to enhance and manipulate fluid transport on superhydrophilic surfaces is particularly valuable for thermal management purposes [35-36]. For example, Courbin *et al.* discovered that the final wetted shape of a spreading droplet (*i.e.,* square, circle, and hexagon) has a strong dependence on the geometric parameters of the topographic features and the intrinsic contact angle [37]. Sbragaglia *et al.* [38] and Pirat *et al.* [39] found that the rate of propagation of the liquid is typically larger in the direction parallel to the liquid front compared to the direction perpendicular to the liquid front, and depends on the geometry of the pillars and the intrinsic contact angle. In the previously reported work, the liquid propagated with a liquid layer of uniform thickness across the structured surfaces. The ability of controlling liquid in the third dimension, *i.e.*, the thickness, has not been achieved while it is actually very important in thin film evaporation because the thermal resistance is proportional to the thickness of the liquid film. However, in this work during the propagation of liquid on nanostructured surfaces, a new phenomenon was discovered where defined nanostructure geometries during the spreading process cause the liquid to separate into multiple layers with varying thicknesses. Meanwhile, an analytical model was developed to interpret this separation of the liquid and fabricated additional structures to validate the proposed model.

Fabrication of nanostructures

The nanostructures used in the experiments are nanopillars arrays. The pillars ranged in diameters from 500-800 nm and spacings from 500-800 nm, and were fabricated by projection lithography and deep reactive ion etching (DRIE). The fabrication process is shown in Fig. 2-1.

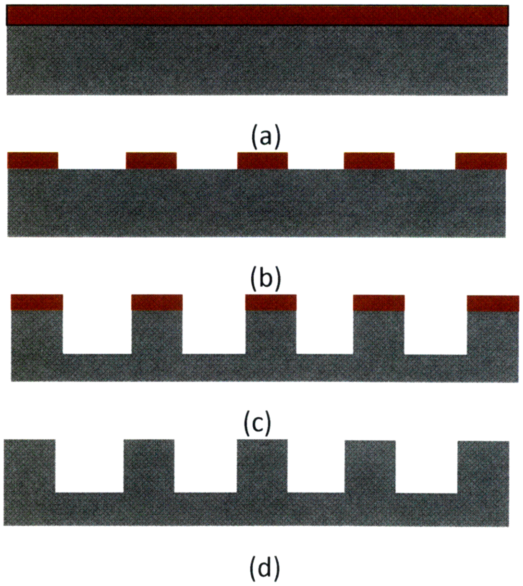

Fig. 2-1 The fabrication process of nanopillars. (a) Silicon wafer coated with photoresist. (b) Coated wafer exposed and developed to reveal the feature. (c) Silicon wafer etched to desired depth. (d) Photoresist was stripped to finish the fabrication.

The fabricated nanopillars are as shown in the scanning electron micrograph in Fig. 2-2.

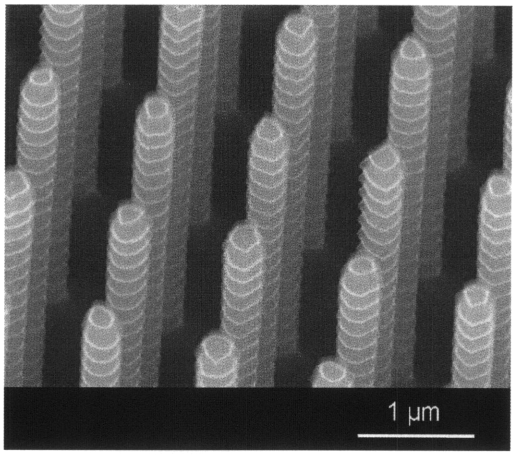

Fig. 2-2 Scanning electron micrograph of a surface with nanostructured arrays of pillars with diameters of 500 nm and spacings of 800 nm. The scallops have dimensions of approximately 100 nm.

Multi-layer Spreading Phenomenon

When a 2 μL droplet of de-ionized (DI) water was deposited onto these surfaces, the liquid separated into several layers. A lower layer advanced first, and subsequent sequential layers followed on top of the first one. The phenomenon shown in Fig. 5, was visualized with fluorescent microscopy with a 40× magnification (NA=0.60). A 29 mM Rhodamine B solution was used to enhance the contrast between the visualized layers. (A movie of the multi-layer spreading behavior is provided in supplementary materials S1_Spreading.mpg).

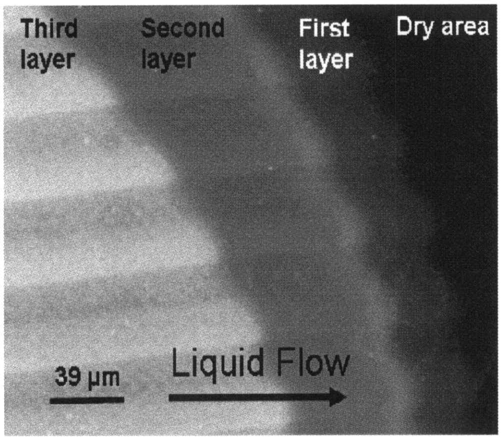

Fig. 2-3 Visualization of multi-layer spreading on the corresponding geometry in Fig. 4. Liquid spreads from left to right where the dark area is dry. The differences in intensity indicate variations in liquid film thickness.

Similar multi-layer phenomena during the receding process were also observed but are not shown here for brevity. The observed horizontal stripes are an optical effect due to slight variations in pillar diameter. To find out the reason for the separation, pillar arrays with varying parameters such as different shape (e.g. circular or square), varying size (diameters ranging from 500 nm to 5 µm) and different sidewall roughness (with or without visible scalloped features). The SEMs of the control group pillars are as shown in Fig. 6. It turns out that the multi-layer separations are positively correlated to the presence of the scalloped features. The separation remains regardless of the shape or size of the pillars. However, when pillar arrays with the same diameter and spacing were fabricated with non-visible scalloped features, the liquid spread across the surface with a uniform film thickness. These observations motivated me to develop a surface-energy-based model to predict liquid separation induced by the fine structures on the nanopillars.

Varying shapes of nano pillars (Circular or Square)	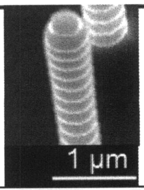	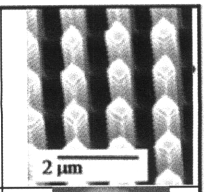
Varying size of pillars (diameter d=500 nm-3.5 µm)	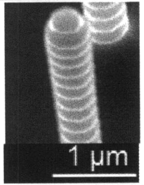	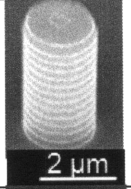
Varying sidewall roughness	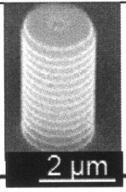	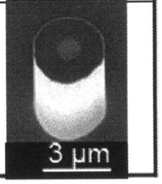

Fig. 2-4 Pillars with varying parameters to find the cause of multi-layer separation.

Modeling

In the model, the scallops are idealized into tiered steps as shown in Fig. 2-5(a). The parameters h_u, h_l, d_u, d_l are the upper and lower height, and the upper and lower diameter, respectively. Fig. 2-5(b) shows the normalized change in surface energy as a function of the normalized liquid height. Because the pillars are hydrophilic, a higher liquid height typically corresponds to a lower surface energy as shown between state (i) and state (ii), as well as between state (iii) and state (iv). However, when a horizontal surface is present, an energy barrier exists as shown between state (ii) and state (iii). In this case, when the liquid covers the surface, the amount of surface energy gained from the solid-liquid and liquid-air interfaces is greater than the surface energy lost due to the reduced solid-air interface. A similar energy barrier is present between state (iv) and state (v), which maintains the liquid below the top of the pillars. Fig. 2-5(b) shows a particular configuration with naturally oxidized silicon pillars with an intrinsic contact angle of 38 degrees, and with h_u=h_l and d_u =0.7d_l. The size of the energy barrier between state (ii) and state (iii) scales with the intrinsic contact angle and 1-$(d_u/d_l)^2$. Therefore, for pillars of the same material (same intrinsic contact angle), a decrease in the d_u/d_l ratio will increase the size of this energy barrier such that state (iv) can have a higher energy than state (ii). One example of such a case is shown in Fig. 2-5(c), when h_u=h_l

and d_u =0.5d_l. The difference of the normalized energy between state (ii) and state (iv) plays an important role in the separation phenomena, which is determined by

$$
\begin{aligned}
S = {} & \gamma_{LV} \frac{1}{h_u + h_l}\left(\frac{1}{\Lambda_1} - \frac{1}{C}\right) \\
& - \gamma_{LV} \frac{1}{h_u + h_l} \cos\theta \left(\frac{1}{\Lambda_1} - \frac{1}{C}\right) - \gamma_{LV} \frac{1}{l} \cos\theta \left(\frac{\pi A (C + B(1-C))}{\Lambda_2} - \frac{\pi A}{1 - \frac{\pi A^2}{4}}\right)
\end{aligned}
\qquad (2\text{-}1)
$$

where $\Lambda_1 = (1-C) + \frac{(1-\frac{\pi A^2}{4})}{(1-\frac{\pi A^2 B^2}{4})} C$, $\Lambda_2 = (1-\frac{\pi A^2 B^2}{4})(1-C) + (1-\frac{\pi A^2}{4})C$,

$A=d_l/l$, $B=d_u/d_l$, $C=h_l/(h_u+h_l)$, l is the distance between the centers of neighboring pillars, and θ is the intrinsic contact angle of the liquid on the solid. The details of the derivation are provided in Appendix A. When the liquid is deposited onto the surface as shown in Fig. 2-5(d), the liquid chooses the configuration with the lower surface energy. If S<0, the energy of state (ii) is lower than that of state (iv), and when a small volume of liquid, ΔV, is supplied from the droplet in this case, the liquid propagates at the edge as a separated layer (Fig. 2-5(d) left configuration). In contrast, when S>0, state (iv) is preferred because it has the lowest energy and the liquid remains in a uniform layer at the height of the pillars (Fig. 2-5(d) right configuration).

The analytical curve for S=0 as calculated from Eqn (2-1) is plotted in Fig. 2-6(b) and Fig. 2-6(c). For the case considered, γ_{LV} =0.072 N/m and ϑ=38 degrees (where the contact angle was measured for a smooth naturally oxidized silicon surface with a goniometer). The cases for Fig. 2-6(b) and Fig. 2-6(c) differ in the location of the lower edge, resulting in C=0.63 and C=0.49, respectively. These two cases were chosen to facilitate a comparison with the experiment described below. The S=0 curve demarcates the boundary between single-layer and dual-layer spreading in the parameter space of A and B.

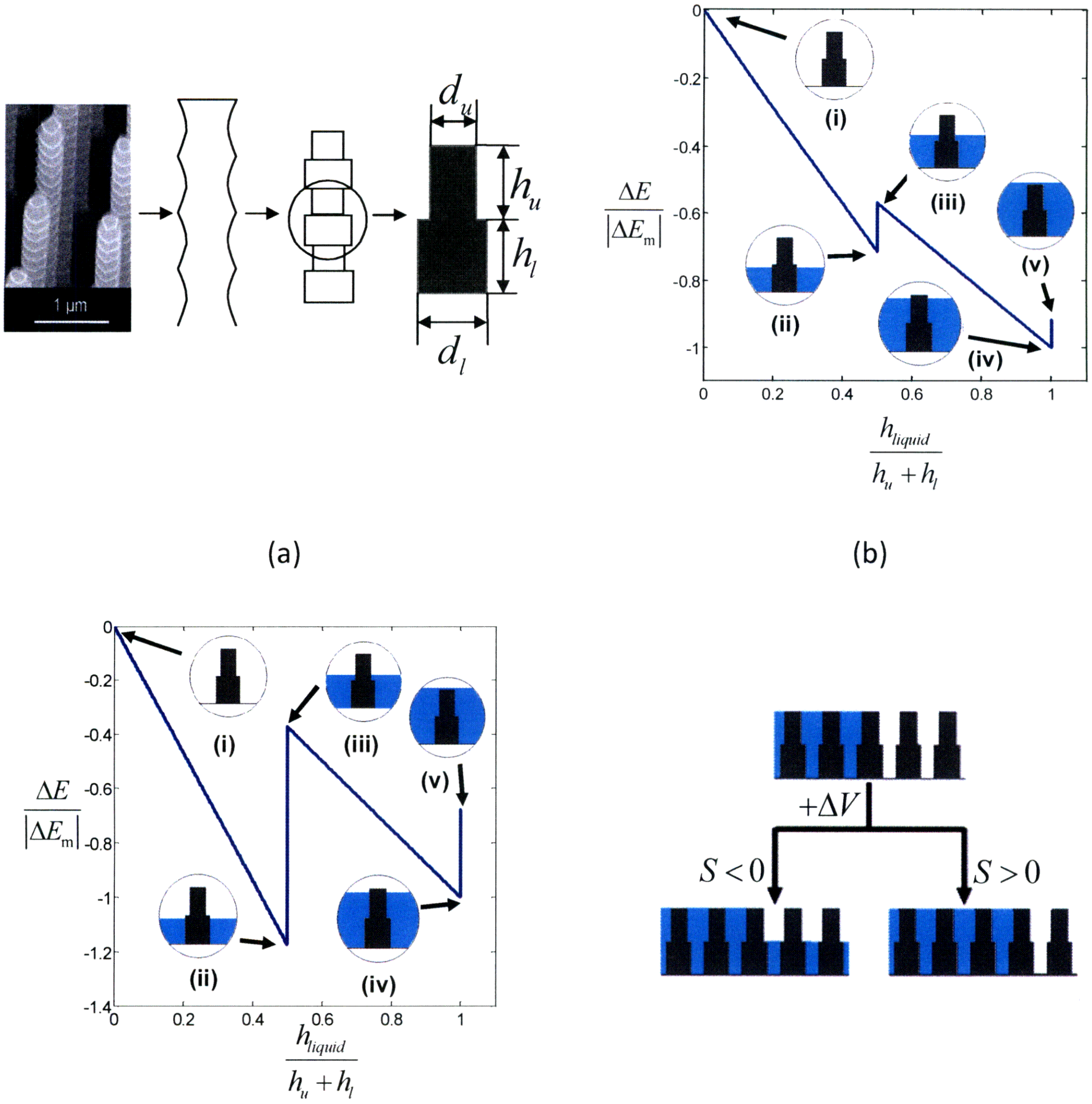

(a)

(b)

(c)

(d)

Fig. 2-5: (a) Schematic showing the idealization of the scalloped pillars from the DRIE process into tiered steps. (b) The change in normalized surface energy as a function of normalized liquid height on a two-tiered pillar geometry where h_u=h_l and d_u=0.7d_l. E_m is the energy change when the liquid wets the entire pillar and h_{liquid} is the height of the liquid interface. (c) The change in normalized surface energy as a function of normalized liquid height on a two-tiered pillar geometry where h_u=h_l and d_u=0.5d_l. (d) Schematic showing a liquid droplet deposited onto the surface and the two possible spreading configurations determined by the parameter, *S*, when a volume of ΔV is supplied from the droplet.

Experimental Validation of the Model

To validate the model, additional pillars with a single notch of defined size, d_u, and location, h_l were fabricated (Fig. 2-6(a)). The etching recipe is provided in the Appendix B. The total height of the pillars is 5 µm. The lower diameter, d_l, ranges from 2 µm to 3.5 µm while the distance between pillars, l, ranges from 2 µm to 7 µm, yielding a variation in parameter A from 0.2 to 0.7. However, d_u, and hence the parameter B, is limited to a range of 0.7 to 0.9 from the availability of existing DRIE capabilities. We fabricated the notch at two heights: 3.15 µm and 2.45 µm, which resulted in C=0.63 and C=0.49, respectively. SEM images of representative pillars with a single notch are shown in Fig. 2-6(a). The working liquid used was DI water. The experimental results are overlayed with the model predictions in Fig. 2-6(b) and Fig. 2-6(c). The cases where dual layers appeared in both advancing and receding process are specified as circles. Interestingly, we observed that for certain pillar geometries, dual-layer separation occurred only during the receding process, and not during the advancing process. These cases are labeled as triangles. Pillar geometries in which the liquid advanced and receded in a uniform layer are labeled as squares.

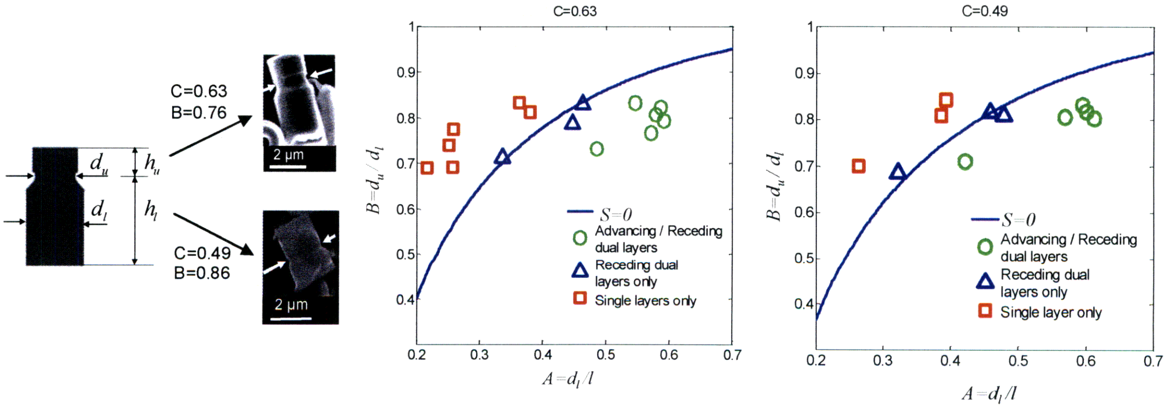

(a) (b) ©

Fig. 2-6 (a) Schematic showing pillars with a single notch and associated dimensions. Representative SEMs are shown for the cases when C=0.63 and B=0.76 and C=0.49 and B=0.86. (b) The parameter space that determines the presence of a single layer or dual layers for the case C=0.63. Experiments with pillars of diameters ranging from 2 µm to 3.5 µm and spacings of 2 µm to 7 µm are plotted. (c) Parameter space that determines the presence of single or dual layers for the case C=0.49. The range of diameters and the spacings are the same as in (b).

The experimental results show that the theoretical curve well demarcates the boundaries between geometries that lead to separated layers, and those that lead to a single layer, for both the advancing and receding processes. However, close to the boundary (S=0), liquid separation occurs only in the receding process (the triangles).

This result is expected as briefly explained below. The analytical model we developed only accounted for surface energy. However, in our experiment, when the droplet was deposited, the Laplace pressure from the positive curvature of the droplet also contributed to the advancing process of the liquid. As a result, the liquid has a higher kinetic energy which enables the liquid to overcome the energy barrier for S close to zero. In the receding process, the liquid evaporated and receded slowly; the liquid is thus only driven by surface tension and leads to liquid separation. Liquid separation is, therefore, well-predicted by the theory. The spreading behavior for geometries far from the boundary is not affected by the additional effect of the Laplace pressure and the model is considered accurate in predicting both advancing and receding behavior.

Conclusion

In summary, nanoscale pillars with scallops of particular geometries can induce energy barriers that lead to a disruption of the liquid upon spreading, forming multi-layer liquid films. A model based on surface energy was developed to explain the observations. Despite the idealizations that were made on the geometry, the theoretical prediction provides good agreement with the experimental observations. The results suggest that the spreading behavior can be controlled by choosing proper pillar geometries, which offer possibilities to control the thickness of liquid films on textured surfaces.

Chapter 3: Planar Liquid Propagation on Micropillar Arrays

Washburn's Model

The heat removal rate is proportional to the velocity of the liquid in the thin film, as shown in Eqn.1-1 in Chapter 1. Therefore, the propagation rate of the liquid within the pillar arrays needs to be well-controlled and predicted for thermal management applications. The propagation rate is determined by the balance between the capillary driving force and the viscous resistance. Capillary driven flow in simple tubes was first proposed with Washburn's Model [40] as follows:

$$V = \frac{dx}{dt} = \frac{w\gamma\cos\theta}{6\eta}\frac{1}{x}$$

$$\therefore x = \sqrt{\frac{w\gamma\cos\theta}{3\eta}t} \qquad (3\text{-}1)$$

where *V* is the propagation velocity, *x* is the propagation distance, *t* is the propagation time, *w* is the width of the tube, η is the dynamic viscosity of the liquid, γ is the surface tension of the liquid, and θ is the contact angle of the liquid on the material of the tube. However, with pillar arrays, neither the driving force nor the viscous resistance can be easily calculated with an analytical model. Numerical simulations can conveniently determine the viscous resistance when the geometries are all provided. However, in practice, design guidelines are needed to optimize the geometries to maximize the propagation rate, which cannot be achieved by numerical simulation. Thus a semi-analytical model, which is called "Modified Washburn's Model" was developed and validated with experimental data.

Modified Washburn's Model

To predict the propagation velocity in the pillar arrays, the capillary force and viscous resistance need to be quantified. Due to the complex geometry, an energy-based approach is used to determine the capillary pressure:

$$\Delta P_{cap} = \frac{\Delta E}{\Delta V} = \frac{\gamma_{LV}(l^2 - 0.25\pi d^2)(\cos\theta - 1) + \gamma_{LV}\cos\theta\pi dh}{l^2 h} \tag{3-2}$$

where ΔE is the change in surface energy when the volume of the liquid film changes by ΔV .The height, diameter and center-to-center distance of the pillar array are given by *h, d, l*, respectively. The surface tension of the liquid is γ_{LV} , and the contact angle of the liquid on the solid is θ.

The viscous resistance, however, is more difficult to calculate. For simpler geometries such as rectangular grooves, there are empirical equations to determine the pressure drop along the groove [41]:

$$\Delta P_{vis} = \frac{2\mu\beta x \frac{dx}{dt}}{D_h^{\ 2}}(f\,\mathrm{Re}_{l,h}),\quad D_h = \frac{4D_g W}{2D_g + W},\quad \beta = \frac{W}{l} \tag{3-3}$$

$$f\,\mathrm{Re}_{l,h} = 24(1 - 1.3553\alpha + 1.9467\alpha^2 - 1.7012\alpha^3 + 0.9564\alpha^4 - 0.2537\alpha^5),\quad \alpha = \frac{W}{D_g}; \tag{3-4}$$

where *W* is the width of the groove, D_g is the depth of the channel, and *l* is the period of the grooves, as shown in Fig.3-1.

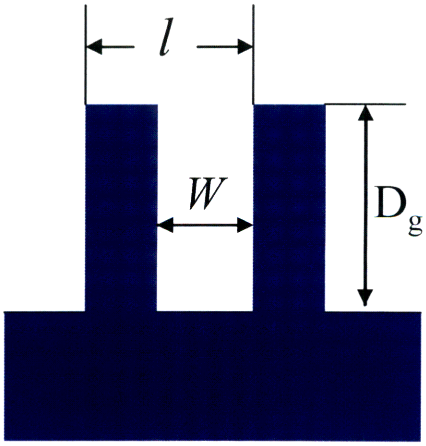

Fig. 3-1 Schematic showing the geometry of rectangular grooves

Based on this empirical equation, the spacings between the circular pillars are approximated by a series of rectangular grooves with varying widths, as shown in Fig.3-

2. Such approximations are considered valid because the Reynolds number of the flow at this scale is very small and the flow is highly viscous. In this case, the pressure drop across the pillars can be determined by summing up all of the pressure drops in each of those rectangular sections.

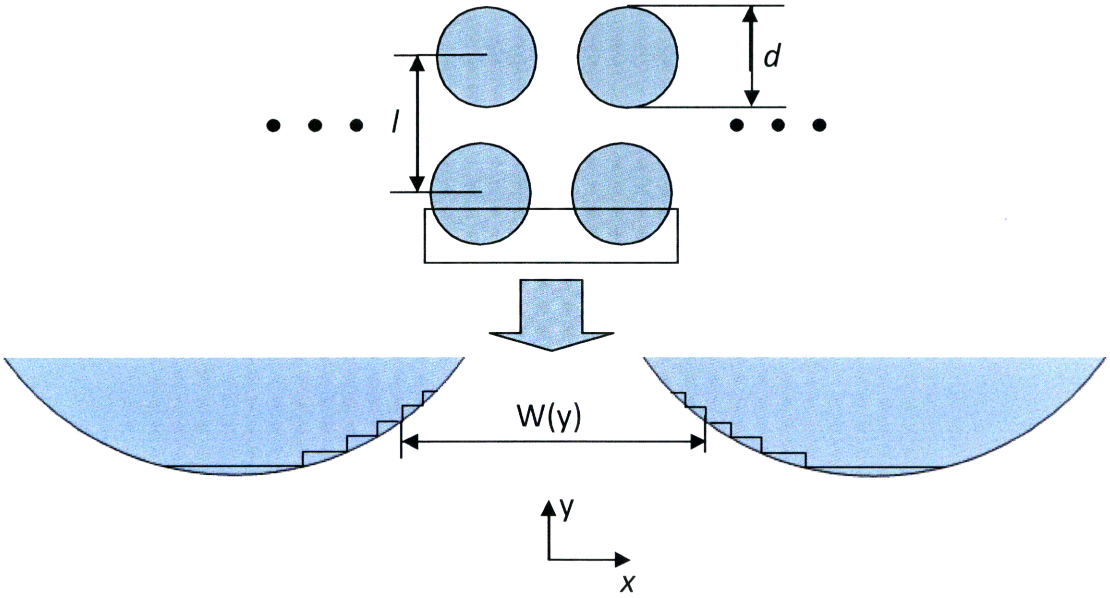

Fig. 3-2 Schematic showing an approximation of circular pillars to a series of rectangular grooves. The width of the grooves, *W*, varies with the position of the grooves (y). The viscous pressure drop across each pillar was calculated by summing up the pressure drop in each of these differential grooves.

MATLAB was used to determine the total pressure drop across one pillar with a given velocity v_0 and the geometry. The code is provided in Appendix C. Assuming such a pressure drop is dP_0 and that the pressure drop is proportional to the velocity and the propagation distance, then the viscous pressure drop is given by:

$$\Delta P_{vis} = KV\frac{x}{l} = K\frac{x}{l}\frac{dx}{dt}, \tag{3-5}$$

where *k* is the pressure drop coefficient defined as $K=dP_0/v_0l$. The propagation distance, propagation velocity and center-to-center distance of the pillar array are given by *x*, *V* and *l*, respectively. Therefore, the propagation distance as a function of time is determined by combining the results with Eqn (3-4):

$$\Delta P_{vis} = k\frac{x}{l}\frac{dx}{dt} = \Delta P_{cap} = \frac{\gamma_{LV}(l^2 - 0.25\pi d^2)(\cos\theta - 1) + \gamma_{LV}\cos\theta\pi dh}{l^2 h}$$

$$\therefore \frac{dx}{dt} = \frac{\gamma_{LV}(l^2 - 0.25\pi d^2)(\cos\theta - 1) + \gamma_{LV}\cos\theta\pi dh}{klh}\frac{1}{x}$$

$$\therefore x = \sqrt{2\frac{\gamma_{LV}(l^2 - 0.25\pi d^2)(\cos\theta - 1) + \gamma_{LV}\cos\theta\pi dh}{klh}}\sqrt{t} \tag{3-6}$$

The curves corresponding to Eqn (3-6) are plotted in Fig. 3-5 with a dash line.

Experimental Validation

To validate Modified Washburn's Model, pillar arrays with diameters ranging from 2.58 µm to 3.85 µm and spacings ranging from 2.7 µm to 4.95 µm were fabricated with similar fabrication processes described in Chapter 2. The heights of the pillars are 4.96 µm. The experiment setup is shown in Fig. 3-3.

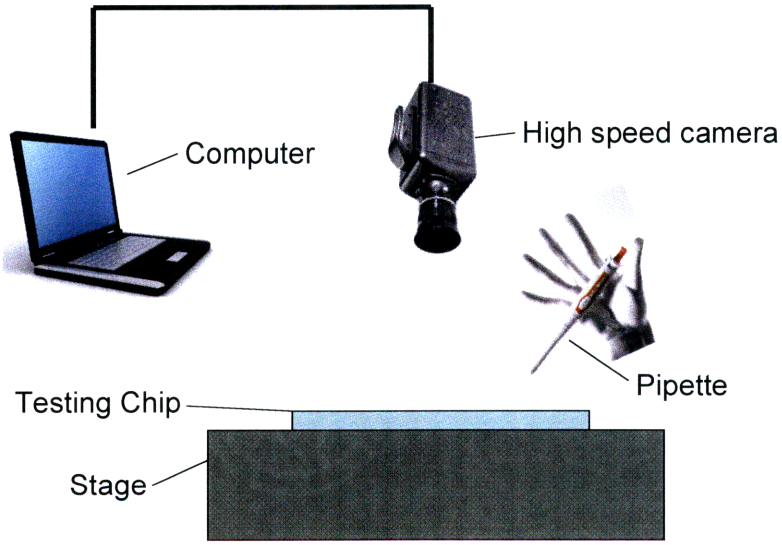

Fig. 3-3 Schematic of the experimental setup for liquid propagation measurements.

In the experiments, a droplet of 2 µL DI water was deposited onto the surface by a pipette. A high speed camera recorded the propagation process of the liquid. Fig. 3-4 shows a series of time-lapse image of the propagation on one of the microstructured surface where the diameter of the pillars is 2.58 µm and the period is 6.96 µm. The experiments on each sample surface were repeated twice and the propagation distances were measured and recorded, as shown by the circles and squares in Fig. 3-5.

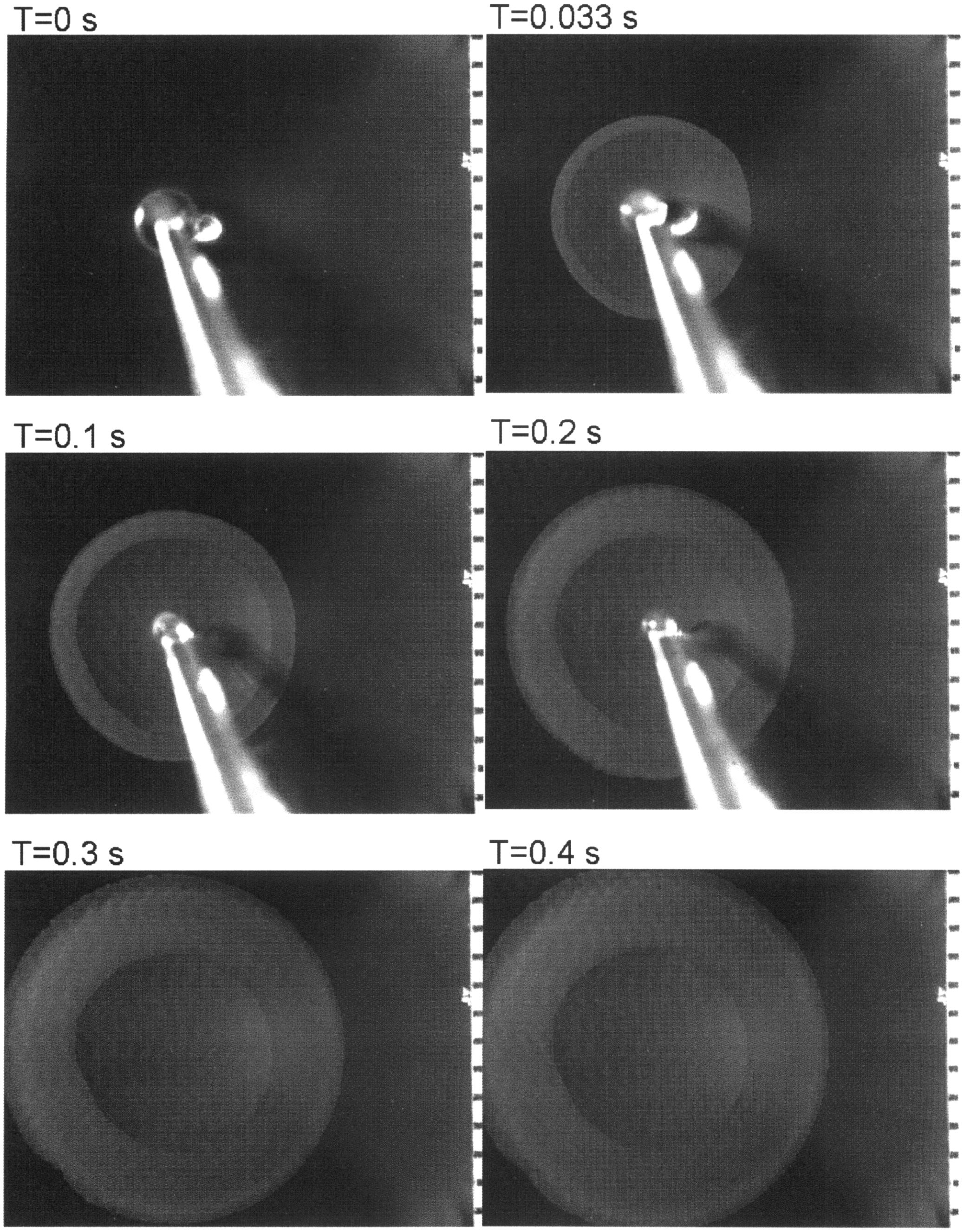

Fig. 3-4 Time lapse images of a droplet of water propagating on a microstructured surface. The surface has micro pillar arrays with diameter of 2.58 μm and spacing of 6.96 μm. On the right side of the images is a ruler where the distance between the bars is 1 mm.

One difficulty in the experiments was that the propagation was almost instantaneous when the droplet reached the surface, such that the starting position and time of propagation was difficult to determine even with a high-speed camera. For example, the starting point was not obtained experimentally in Fig. 3-5 but was calculated with the following approach.

Based on Washburn's Model, the capillary driving force was assumed to be constant and the resistance to be proportional to the propagation velocity and the propagation distance. Under such assumptions, the propagation distance is proportional to the square root of propagation time. Therefore:

$$\begin{cases} x_1^2 = \beta t_1 \\ x_2^2 = \beta t_2 \\ \quad \bullet \\ \quad \bullet \\ \quad \bullet \\ x_i^2 = \beta t_i \end{cases} \tag{3-7}$$

where $\{x_i\}$ are the propagation distances and $\{t_i\}$ are the associated times, which are unknown. In addition, if the differences of two equations from Eqn.3-7 are taken, the relationship is obtained

$$(x_{i+1}^2 - x_i^2) = \beta(t_{i+1} - t_i)$$

$$\therefore (x_{i+1} - x_0) + (x_i - x_0) = \beta(\frac{t_{i+1} - t_i}{x_{i+1} - x_i}) - 2x_0 \tag{3-8}$$

where x_0 is the first point measured in the experiments, which is also unknown. However, the values of x_i-x_0 can be measured. Therefore, a linear fit was used with $\left(\{(x_{i+1} - x_0) + (x_i - x_0)\}, \left\{\frac{t_{i+1} - t_i}{x_{i+1} - x_i}\right\}\right)$ to determine β and x_0. With β and x_0, the experimental data points were fit as shown in a blue solid line in Fig. 3-5.

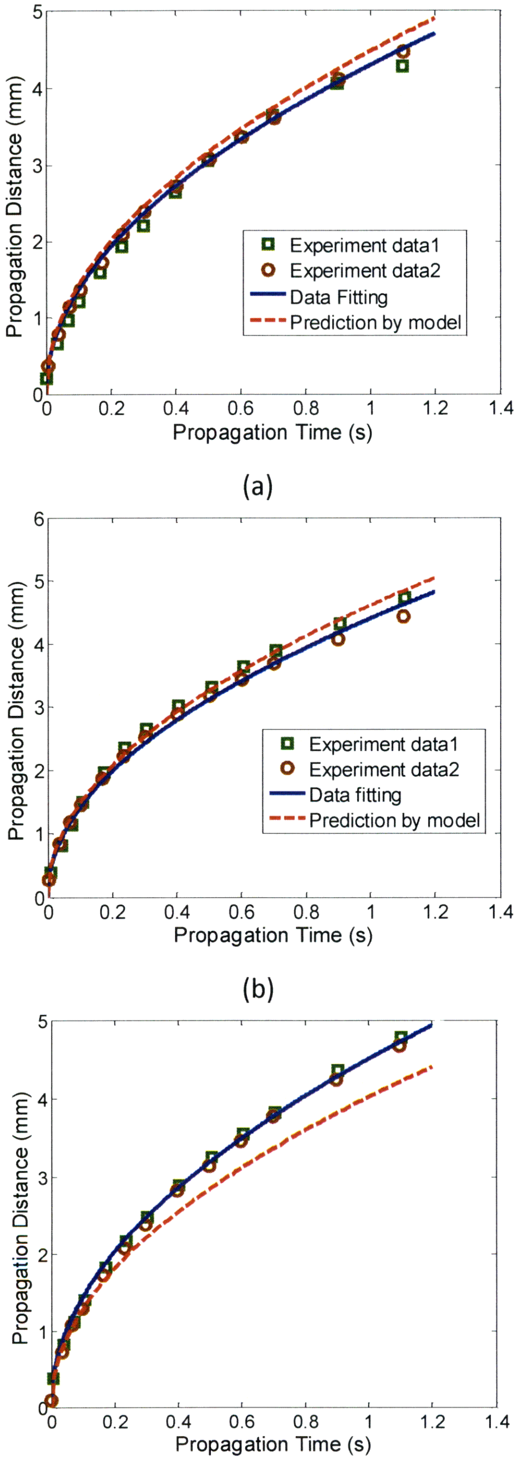

(a)

(b)

(c)

Fig. 3-5 The comparison of experimental data and model prediction of propagation distance as a function of time on micropillar arrays with various geometries. (a) The diameters is 3.25 μm and the center-to-center distance is 8.2 μm. (b) The diameters is 2.58 μm and the center-to-center distance of 6.96 μm. (c) The diameters is 1.95 μm and the center-to-center distance of 7.73 μm.

Fig. 3-5 shows that the model prediction and the experimental data are in good agreement when the porosity of the pillar array, which is defined as the ratio of the spacing of the pillars to the period of the array, *i.e.,* (1-*d*/*l*), is in the moderate range as shown by Fig. 3-5(a) and (b). However, when the porosity is very high, such as the case in Fig. 3-5(c), the model underestimates the propagation rate. Such variation might result from the limitation of the empirical equation adopted in this model, which needs to be investigated further.

Conclusion

In this chapter, a semi-analytical model was developed to predict the propagation rate on circular pillar arrays. Experiments showed that in principal the model can provide accurate prediction of propagation rate when the porosity of the pillar array is moderate. Design guidelines based on the model can be developed with desired liquid film thickness, as will be shown in the next chapter. However, there is considerable variation between the model and experimental data when the porosity is large. Efforts will be made in pursuit of an accurate model over a broader range of geometries in the future.

Chapter 4: Heat Dissipation with Microstructured Surfaces

As discussed in Chapters 2 and 3, the micropillar arrays enable a controlled thin liquid film to propagate on the surface. The propagation velocity is dependent on the geometry as explained in the previous chapter. The heat dissipation rate is dependent on the propagation velocity and the evaporation of the thin liquid layer. In this chapter, the effect of micropillars on thin film evaporative cooling will be discussed. Test devices with micropillar arrays of varying geometries on the front side and resistors, including heaters and temperature sensors, on the back side were fabricated. The heat dissipation capability was demonstrated and as expected, was correlated with the propagation rate of the liquid film.

Design of Test Devices

The design process for the microstructures for heat dissipation is described below. Based on the desired heat flux and the maximum allowable temperature rise, the thermal resistance of the thin film can be determined. The thickness of the liquid film, *h*, is

$$h = kR_{th} \tag{4-1}$$

where R_{th} is the thermal resistance and k is the thermal conductivity of the liquid. The height of the micropillars in this case is the same as the thickness of the liquid film, *h*. In our preliminary experiments, to achieve heat flux as high as 300 W/cm^2 with a temperature rise of no more than 75 °C, the thermal resistance of the liquid film is $R_{th} = \Delta T/q'' = 75/300 = 0.25\ (Kcm^2/W)$. Given that the thermal conductivity for water is 0.58 W/mK, the height of the pillars should be $h = kR_{th} = 0.25 \times 0.58 \times 10^{-4} = 14.5\mu m.$

According to the model developed in Chapter 3, the propagation distance is proportional to the square root of time, which can be written as

$$x = \sqrt{2\frac{\gamma_{LV}(l^2 - 0.25\pi d^2)(\cos\theta - 1) + \gamma_{LV}\cos\theta\pi dh}{klh}}\sqrt{t} \tag{4-2}$$

Thus, the propagation rate as a function of the diameter and the spacing with a given height can be determined, as shown in Fig. 4-1.

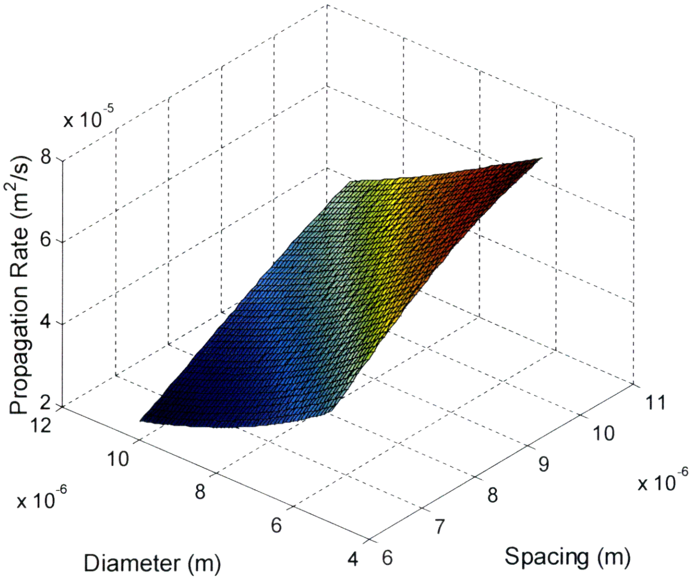

Fig. 4-1 The propagation rate as a function of diameter and the spacing between pillars. The height of the pillars in this case is 14.5 μm.

The results show that micropillar geometries can be optimized to achieve the maximum propagation velocity. In this case, the optimized geometry is 5 μm in diameter with spacings between the pillars to be 10 μm. However, to demonstrate the effect of propagation rate on heat removal rate, pillar arrays with additional geometries were also fabricated. In order to achieve maximum contrast in the propagation velocity and heat removal rate, the geometries were along the line with the largest gradient in Fig. 4-1. In addition, design and fabrication challenges were also considered. Therefore, devices that were fabricated are (in μm): (4, 11), (5, 10), (6, 9), (7, 8), (8, 7), (9, 6), (10, 5), where in each bracket the former number is the diameter and the latter number is the spacing between pillars.

In order to test the heat removal capability *via* thin film evaporation with the fabricated microstructures, the heaters and temperature sensors were integrated into the devices. While there are multiple methods to supply heat and measure temperature, we chose the simple approach of fabricating aluminum resistors on the back side of the chip. By applying voltage to the resistors, the heat flux can be applied by

Joule heating. By measuring the resistances change of the resistors, the temperature can be measured due to the linear temperature dependence of resistivity. The resistors were fabricated through basic lift-off processes with dimensions on the order of hundreds of microns to achieve sub-millimeter spatial resolution and reasonable temperature sensitivity. Doped silicon sensors can provide higher spatial resolution and sensitivity but is much more fabrication intensive.

The contact lithography masks used to define microstructures on the front side, and the resistors on the back side are shown in Fig. 4-2. The pillar arrays on the front side of the wafer are 3 cm by 3 cm, but the whole chip size is slightly larger (4 cm by 4 cm) to enable ease of external connection and handling. The back side of the device has a resistor with a line width of 200 µm spanning the whole chip to provide a uniform heat flux to the entire test device. (This resistor will be denoted as "background resistor" for the rest of this section). Also, there are ten resistors distributed at various positions. The line width of these resistors is 10 µm and the areas of these resistors are 200 µm by 200 µm, which will be denoted as "sensing resistor" for the rest of the section. The line width of the wires connecting the tiny resistors and the contact pads is 50 µm, which is much wider than the sensing resistor itself in order to minimize the connection resistance such that the measured resistance only represents the local temperature. The resistors are fabricated with aluminum because it adheres with silicon very well and the thermal coefficient of aluminum is 0.0039 1/°C in literature [42], which is relatively large.

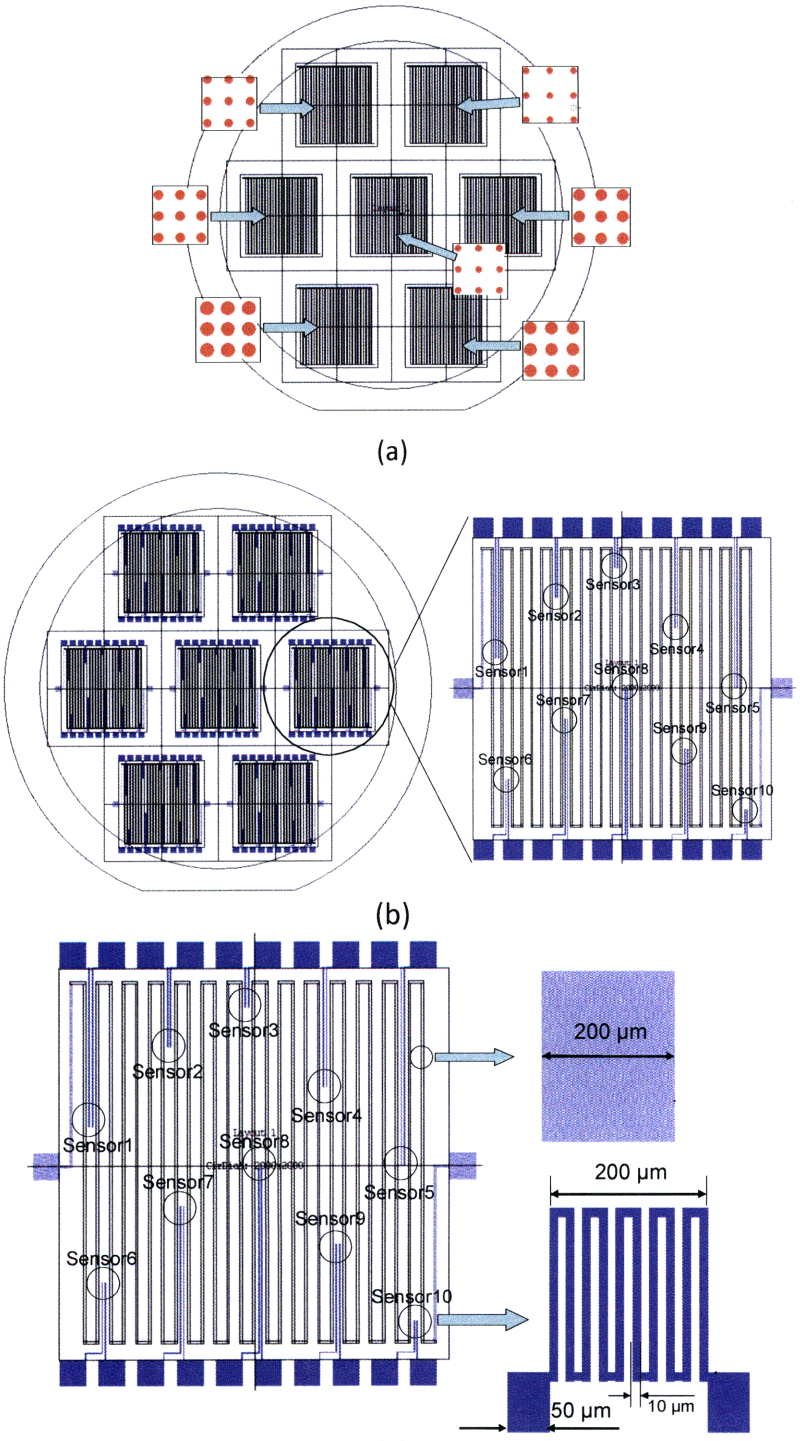

(a)

(b)

(c)

Fig. 4-2 Contact lithography mask layouts for thin film evaporation test devices. (a) The mask layout for the front side of the fabricated test devices. There are seven 3 cm by 3 cm pillar arrays with different geometries, as discussed earlier. (b) The layout for the back side of the fabricated test devices. There are seven identical groups of resistors. (c) The layout for one group of resistors including a large resistor covering 3 cm by 3 cm area and ten smaller resistors, each covering an area of 200 µm by 200 µm. The numbering of the smaller resistors and the line widths of the resistors are also shown.

The thickness of the metal layer can be varied in the fabrication process. In the initial design, the aluminum thickness was chosen to be 300 nm. The resistance value of the background resistors was determined as:

$$R_L = \frac{\rho}{t{\bullet}W} L = \frac{2.82\times10^{-11}}{300\times10^{-9}\times200\times10^{-6}}\times870 = 408.9\ \Omega;$$

The resistance for each sensing resistor is:

$$R_l = \frac{2.82\times10^{-11}}{300\times10^{-9}\times10\times10^{-6}}\times2.2 = 30.68\ \Omega;$$

The resistance of the wire connecting the tiny resistors and the contact pads varies with the position of the resistors. The resistance per millimeter of the connecting wire is:

$$\frac{R_c}{L} = \frac{\rho}{t{\bullet}W} = \frac{2.82\times10^{-11}}{300\times10^{-9}\times50\times10^{-6}} = 1.88\ \Omega/mm$$

The resistor pattern was chosen so that a heat flux pattern with a relatively low and uniform "background" heat flux with several hot spots can be tested, which is very similar to the actual integrated circuit chips.

Fabrication of Test Devices

The test chips were fabricated in the Microsystem Technology Laboratory (MTL) at MIT. The process flow is shown in Fig. 4-3. A more detailed process is included in Appendix D. The images of the fabricated device are shown in Fig. 4-4.

In the fabrication process, there are some variations in the geometries such as the width of the wires and the diameter/spacings of the pillars from the designed value due to the limitations of the photolithography process. Therefore, these parameters needed to be measured after the fabrication.

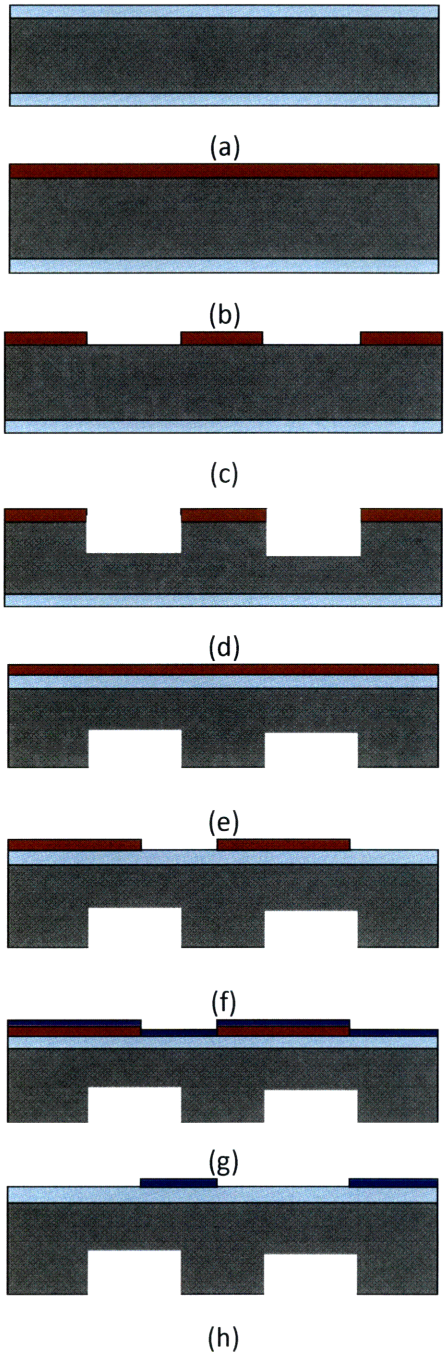

Fig. 4-3 The fabrication process for the test devices. (a) The silicon wafer was oxidized. A SiO_2 layer with the thickness of 100 nm was formed on both sides of the wafer. (b) The SiO_2 layer on the front side was stripped off and photoresist was spun on the front side. (c) After exposure and developing, the pattern was revealed in the photoresist. (d) The wafers were etched to create the pillar arrays on the front side. (e) The remaining photoresist was stripped. The wafers were reversed and a layer of negative photoresist was spun on the back side of the wafers. (f) The photoresist was exposed and developed to reveal the resistor patterns. (g) Aluminum was deposited by E-beam evaporation onto the patterned surface. (h) The photoresist was washed away by acetone. The circuit was formed by the aluminum.

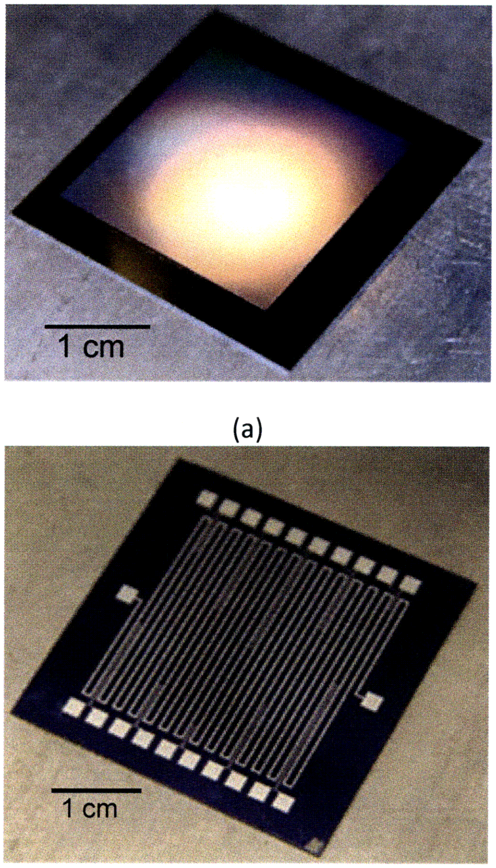

(a)

(b)

Fig. 4-4 The images of the fabricated device. (a) The front side of the device with micropillar arrays. (b) The back side of the device with resistors.

Experiment Setup

The experiment setup is shown in Fig. 4-5. The test chip was mounted on a custom fixture shown in Fig. 4-5(b), which provides electrical connections to the test device to apply the heat flux and extract the electrical signals. There are 22 contact pads on the chip, which makes it difficult to connect with soldering. Thus, pogo pins (Everett Charles Technologies) were used as an alternative. The design of the fixture is shown in Fig. 4-5(b). The fixture was machined from delrin, whose long term working temperature is 90 °C and intermittent working temperature is 140 °C, which is sufficient for the proposed experiments. The fixture was machined by the Central Machine Shop at MIT.

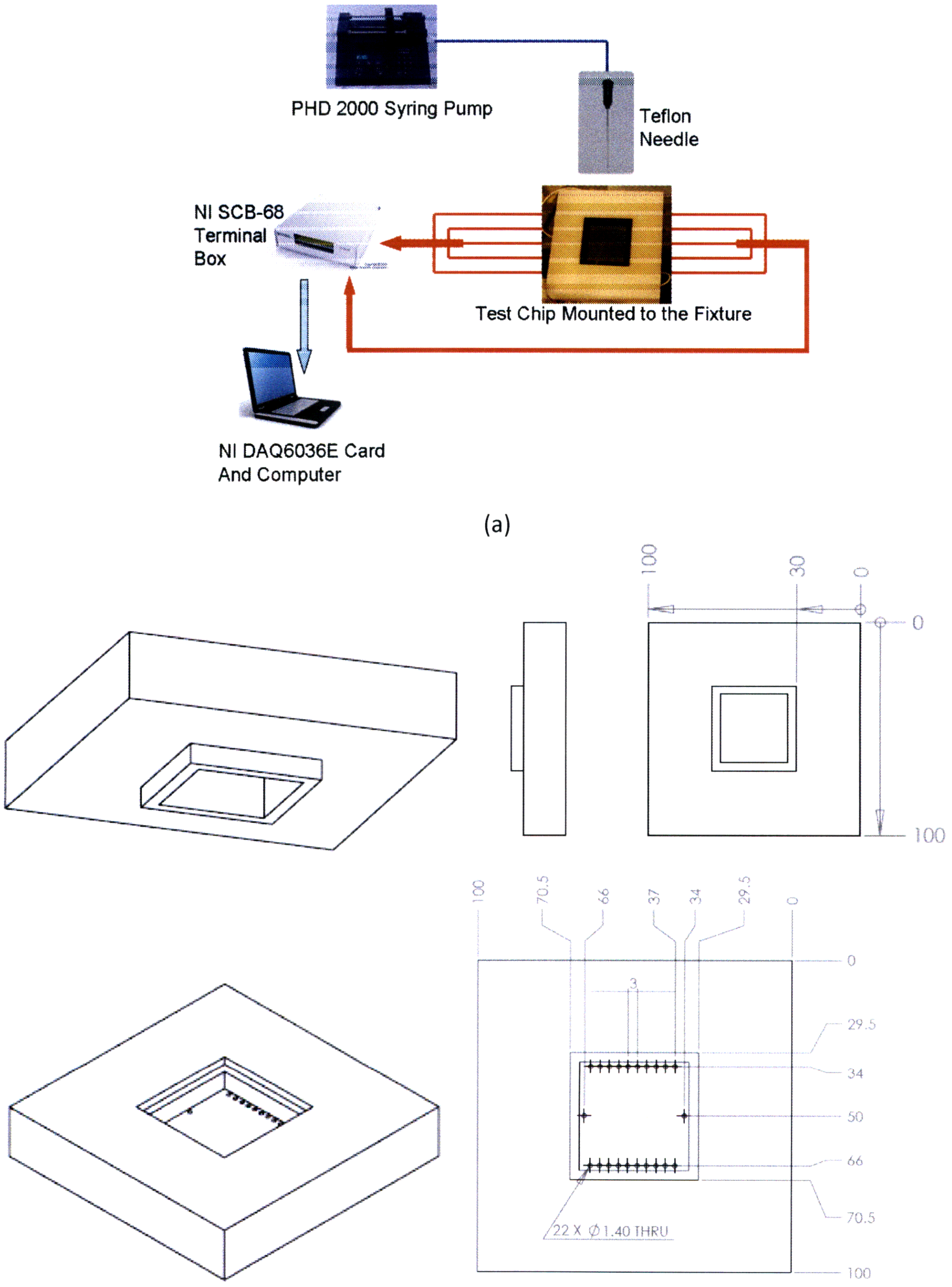

(a)

(b)

Fig. 4-5 The experimental setup. (a) Schematic showing the experimental setup. The liquid was supplied to the chip surface by a PHD 2000 syringe pump through a Teflon needle. The signals were acquired by NI DAQ6036E Card and processed by LabView software. (b) The design of the fixture to mount the chip and connect the chip to external circuits.

A syringe pump (PHD 2000, Harvard Apparatus) with a 100 mL glass syringe was used to supply de-ionized (DI) liquid to the test chip. The outlet of the syringe was connected to 1/8 inch tubing and the tubing was connected to a gauge 24 Teflon needle (Small Parts Inc.) through a luer connector (Hamilton Inc.). The Teflon needle was used to minimize the adhesion of the tip of the needle so that the liquid could detach from the needle more easily. In the experiment, the syringe pump delivered the liquid at a flow rate of 200 μL/min such that droplets detached from the needle tip at a stable rate. The chip was then placed under the needle and the power supply was turned on. Therefore, the heat flux and liquid supply started at the same time.

The resistances were measured with a data acquisition card (DAQ 6036E, National Instruments). The resistors were connected in series with another 15 Ω resistor. A voltage of 0.8 V was applied on the sensing resistors and an external resistor. The voltage across the external resistor was measured and recorded by the LabView. The code for the measurement is included in the Appendix E. The relationship between the measured voltage and temperature will be discussed later.

Temperature Sensor Calibration

The sensors in the fixture were calibrated using a convection oven. When the temperature of the oven reached steady state, by reading an additional thermometer placed in the oven, the voltages across the external resistors, *V*, were recorded. The relation between the resistance of the sensing resistors and the voltage across external resistor is:

$$V = U_{overall} \times \frac{R_{ext}}{R_{ext} + R_t}$$

$$\because R_t = R_0(1 + \alpha T)$$

$$\therefore V = \frac{U_{overall}}{1 + \frac{R_0(1+\alpha T)}{R_{ext}}}$$

$$\therefore \frac{R_0}{R_{ext}} + \frac{R_0 \alpha}{R_{ext}} T = \frac{U_{overall}}{V} \tag{4-3}$$

where $U_{overall}$ is the total voltage applied on the series of the sensing resistor and the external resistor, T is the temperature, R_{ext} is the resistance of the external resistor, R_0 is the resistance of the sensing resistor at zero degree and R_t is the resistance of sensing resistor at temperature T, and α is the thermal coefficient of resistivity.

The sensing sensors were calibrated under five different temperatures: 49, 57, 61, 64 and 70 degree Celsius. The important constants $(\frac{R_0}{R_{ext}}, \frac{R_0\alpha}{R_{ext}})$ were determined by linear regression. For brevity, only the regression figure of Sensor 1 is shown in Fig. 4-6.

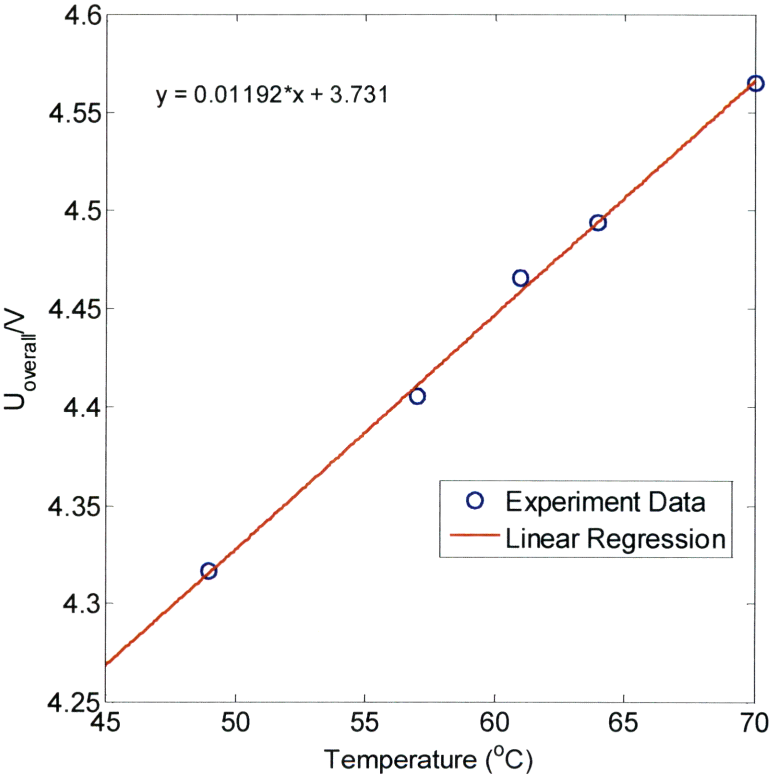

Fig. 4-6 The calibration data and linear regression plot for Sensor 1.

From the linear regression, $R_0 = 3.731R_{ext} = 55.965\ \Omega$ and $\alpha = 0.01192/3.731 = 0.0032(1/^\circ C)$. The same regression process was performed on each of the sensors. However, sensor 3, 5, 8 and 9 have poor electrical connections to the external circuit. Therefore, only the regression results of the sensors that have good connections were obtained as shown in Table 4-1.

	$R_0(\Omega)$	$\alpha(1/^{\circ}C)$
Sensor 1	55.965	0.0032
Sensor 2	76.665	0.0035
Sensor 4	66.530	0.0032
Sensor 6	72.501	0.0033
Sensor 7	59.292	0.0031
Sensor 10	69.287	0.0031

Table 4-1: The regression results for calibration of the sensors with good electrical connections.

The thermal coefficient of resistance was obtained by averaging six sensors: $\alpha = 0.0032\ 1/{}^{\circ}C$. While the temperature coefficient of resistivity for bulk aluminum can be obtained from literature to be 0.0039 1/°C, the measured value was not the same. The difference in the values was due to the fact that the resistor on the chip was fabricated through vapor deposition, which leads to some difference in the lattice structure of aluminum. All the devices were fabricated under the same process parameters, so the thermal coefficient of resistance was considered the same for all of the devices.

Moreover, we can see that the sensitivity of $1/V$ as a function of temperature T is R_0/R_{ext}. As a result, by choosing a smaller external resistor, the sensitivity can be improved. However, if the external resistor is too small, the resistance of the connecting wires, *etc.*, cannot be neglected which may increase the measurement error. Thus in our experiments, the external resistor was chosen to be 15 Ω.

Another method to improve the sensitivity requires increasing the resistance of the sensing resistors by reducing the thickness of the metal layer. However, fabrication of very thin metal layers is difficult using a lift-off process. When the thickness is very small, the metal line can easily have locations of open circuits. In the future, more fabrication runs are needed to optimize the process parameters to create resistors with high resistance on chip. For the experiments demonstrated here, the thickness of the metal layer is 300 nm, which yields resistances approximately from 50-70 Ω.

Experimental Results

In the experiments, the devices were heated up as the liquid was supplied onto the microstructured surfaces. The temperature first rises but finally reaches a relatively stable value, which is termed "final temperature". The same experiment was carried out on five devices with diameters ranging from 3.93 μm to 10.19 μm and spacings ranging from 11.07 μm to 4.81 μm. A typical plot of temperature as a function of time is shown in Fig. 4-7.

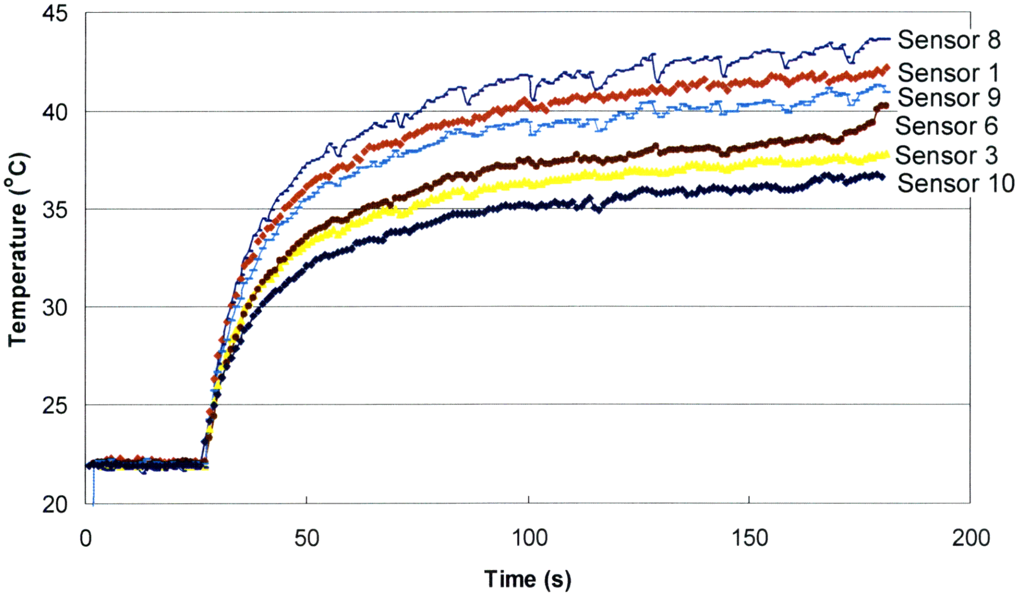

Fig. 4-7 Typical curve of temperature as a function of time. The diameter of the pillars was 9.16 μm and the spacing is 5.84 μm. The heat flux by the background resistor is 0.472 Watts per square centimeter. The water flow rate was 200 μL/min.

When the applied heat flux was low, liquid formed a uniform thin layer on the surface of the chip, as shown in Fig. 4-8(a). Because the liquid was not supplied in a continuous stream but in discrete drops, there were occasional dry areas near the edge of the chip or a large droplet at the center of the chip, which led to a difference in temperatures of different sensors. As a result, the temperatures of sensors near the center of the chip, such as Sensor 3, Sensor 6 and Sensor 10, were usually lower while the temperatures measured by sensors near the edge, such as Sensor 1, Sensor 5 and Sensor 8, were usually higher, which can also be seen from Fig. 4-7. Similar phenomena were also observed on other test devices.

As the heat flux was increased, the pattern of the liquid film changed due to the increasing evaporation rate of the liquid. However, the heat flux was limited by the propagation rate of liquid in the microstructures. Dry areas initiated at the edges of the chip, as shown in Fig. 4-8(b). When the heat flux was further increased, the dry areas increased where finally the whole chip surface dried out, as shown in Fig. 4-8(c). Before liquid dry-out occurred, there was little temperature rise of the chip with significant increases in heat flux. Once liquid dry-out was reached, the temperature rose by over 20 °C. The temperature of the chip as a function of time with increasing heat flux is plotted in Fig. 4-9. Initially the voltage applied on the heater was 60 V, providing a heat flux of 1.3 W/cm^2. At each arrow, the voltage was increased by 5 volts. The highest voltage applied was 85 V, providing the maximum heat flux of 2.7 W/cm^2.

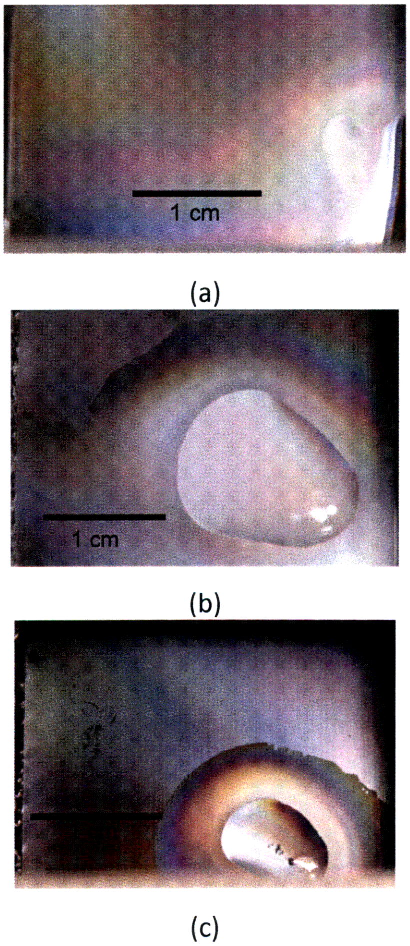

Fig. 4-8: The behavior of the liquid film as the heat flux increases. (a) The liquid forms a uniform thin film when the heat flux is 1.3 W/cm^2. (b) Dry areas start to develop near the corner and the edge of the chip as the heat flux increases. (c) Dry out occurs. The liquid film can only cover a small area. Bubble nucleation occurs as the droplet hits the surface.

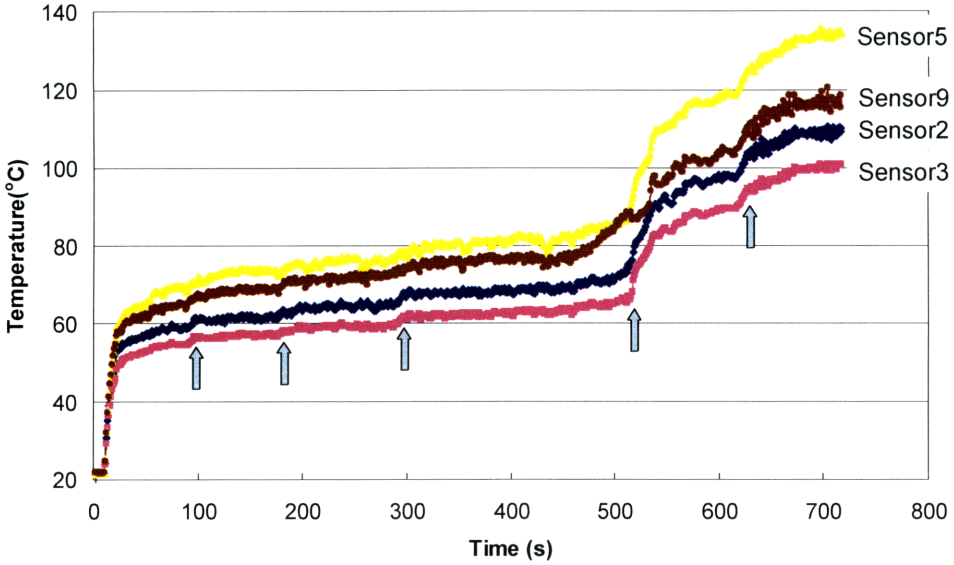

Fig. 4-9 Chip surface temperatures as functions of time with increasing heat flux. Initially the voltage applied on the heater was 60 V, providing a heat flux of 1.3 W/cm^2. At each arrow, the voltage was increased by 5 V. There was a jump in the temperature at the fourth arrow where dry out occurred at the heat flux of 2.3 W/cm^2.

The same experiments were repeated for different geometries. The final temperatures as a function of heat flux were measured, as shown in Fig. 4-9. While there are temperature variations in Fig.4-9, the lowest temperatures are shown in Fig. 4-10.

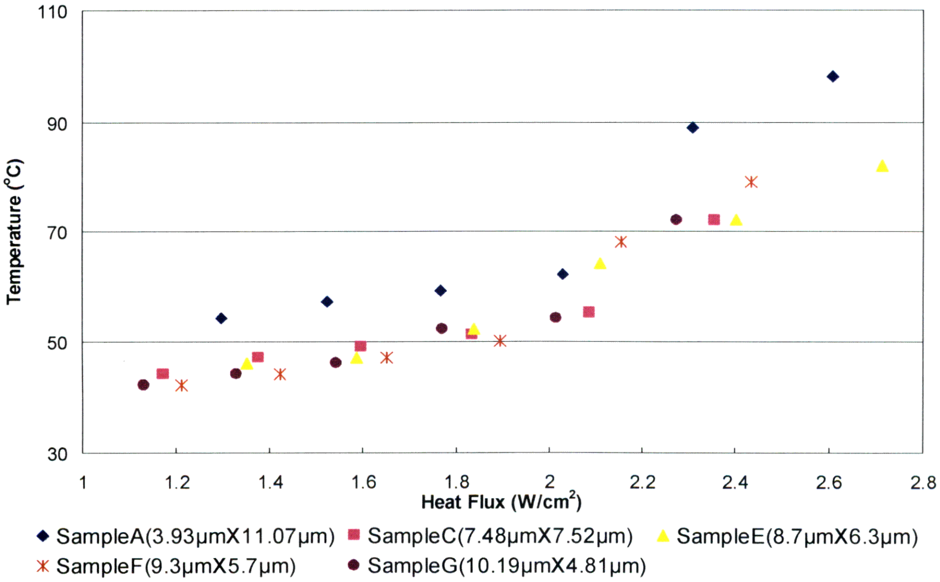

Fig. 4-10 The final temperature as a function of heat flux on various samples.

Analysis

From the experimental results and the visual observations, the relationship between the final temperature of the chip and the heat flux under a fixed liquid flow rate can be summarized with the behavior shown in Fig. 4-11.

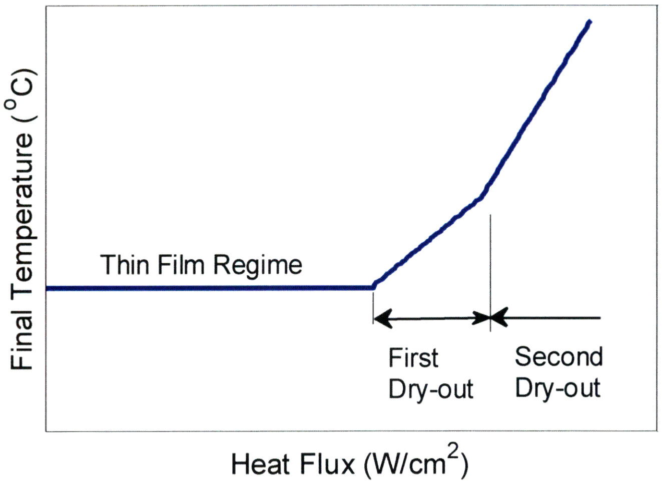

Fig. 4-11 Typical behavior of final temperature on a chip as a function of heat flux.

When the heat flux is below a certain point, the liquid can form a thin film on the chip as in Fig. 4-8(a), and the temperature is low and insensitive to the change in heat flux, denoted by the horizontal part of the curve in Fig. 4-11. However, under higher heat fluxes, the dry areas start to develop, which is denoted as the "First Dry-out" in Fig. 4-11. The onset of First Dry-out is dependent on the propagation rate of the liquid on the microstructured surface. When the heat flux is further increased, the droplet of liquid will completely vaporize before the next droplet reaches the surface. Thus, there is a period of time when the surface is completely dry, denoted as "Second Dry-out", which is dependent on the liquid flow rate. Fig. 4-9 and Fig. 4-10 show that when dry-out occurs, the temperature rises significantly. Second Dry-out can be avoided by increasing the liquid supply rate. The goal of optimization of the microstructures is to avoid First Dry-out from occurring.

In the experiments, however, the temperature measurements were carried out only on discrete heat flux values (where the voltage applied on the heater was increased in 5 V increments). As a result, the occurrence of First and Second Dry-outs were not accurately located. However, combined with visual observation, the onset of the Dry-outs can be roughly estimated. The location of the First Dry-out on Sample G, where the pillar diameter is 10.19 μm and the pillar spacing is 4.89 μm, was estimated to be between heat fluxes of 1.54 W/cm^2 and 1.77 W/cm^2. While on Sample E, where the diameter is 8.7 μm and the spacing is 6.3 μm, the First Dry-out occurred at heat flux between 1.83 W/cm^2 and 2.11 W/cm^2, which is higher than on Sample G. The results are expected because according to Modified Washburn's Model, the propagation rate on Sample E should be higher than on Sample G. As a result, the microstructures on Sample E can supply more liquid to the entire chip surface, and avoid the development of dry areas.

Another interesting phenomenon observed in the experiments is that the final temperature of Sample A was significantly higher than the other samples even under the same heat fluxes. The result was unexpected because we initially assumed that the thermal resistance of thin film evaporation was solely caused by the conduction in the liquid film, which implies that the thermal resistance should be the same for all samples. However, the experiments showed that the final temperatures on Samples C, E, F and G were approximately the same and lower than Sample A. The explanation for these results is as follows. In the schematic in Fig. 4-12, heat flows in two direction: by conduction in the liquid film and through the pillars which act as pin fins. The thermal resistance network based on the schematic is also shown in Fig. 4-12. When the pillars are far away from each other, the heat flow through the pillars can be neglected. However, in our experiments, the spacings between the pillars are all smaller than the thickness of the liquid film which suggests the fin effect from the pillars cannot be neglected.

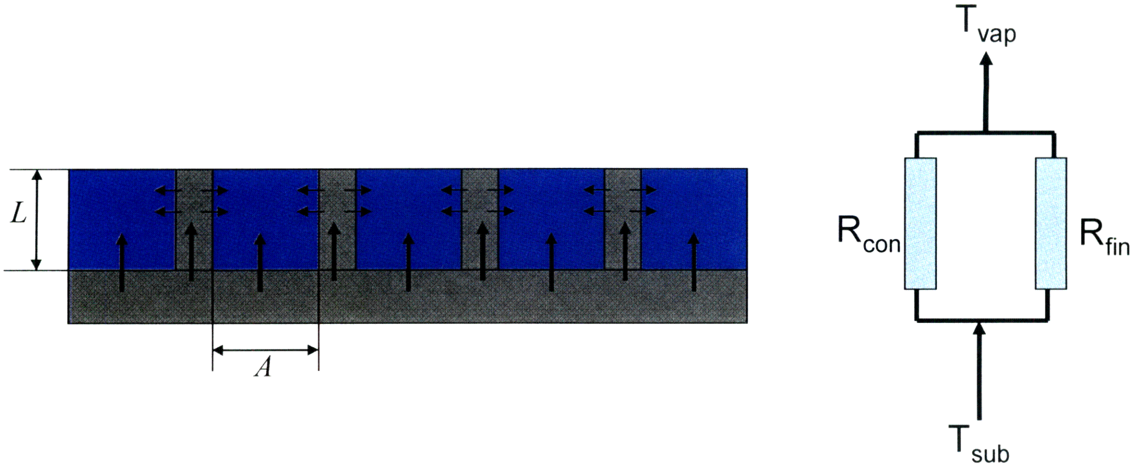

(a) (b)

Fig. 4-12 (a) Schematic showing the heat flows in the thin film considering the presence of pillars. (b)The overall thermal resistance network.

The convection resistance through the liquid film is given by:

$$R_{con} = \frac{1}{h_c A} \tag{4-4}$$

where *A* is the area of the liquid film, h_c is the convection heat transfer coefficient between the pillars and the liquid.

With the fabricated pillar geometries, the thermal resistance of the fin is given by:

$$\begin{aligned} R_{fin} &= \frac{1}{(h_c P / \beta)\tanh \beta L} \\ \beta &= \sqrt{h_c P / k' A_c} \end{aligned} \tag{4-5}$$

where *P* is the perimeter, *L* is the length of the fin which is the same as the thickness of the liquid film, A_c is the cross section area of the fin, *k'* is the conductance of the pillars, As shown in Fig.4-12, the fin thermal resistance and the conduction thermal resistance are connected in parallel. The overall thermal resistance is:

$$R = \frac{1}{\dfrac{1}{R_{con}} + \dfrac{1}{R_{fin}}} = \frac{1}{h_c A + \dfrac{h_c P}{\beta}\tanh \beta L} = \frac{1}{h_c} \bullet \frac{1}{A + \dfrac{P}{\beta}\tanh \beta L} \tag{4-6}$$

Given the diameters and spacings of the different pillar arrays in this study, the thermal resistance of the thin film on Sample A, C, E, F and G are shown in Table 4-2:

Sample	Geometries (Diameter X Spacing, µm)	Thermal Resistance (K/W·cm^2)	Experimental Thermal Resistance at the Lowest Heat Flux (K/W·cm^2)
A	3.93 X 11.07	$57.4/h_c$	23
C	7.48 X 7.52	$43.1/h_c$	17.1
E	8.7 X 6.3	$40/h_c$	16.3
F	9.3 X 5.7	$38.8/h_c$	15.92
G	10.19 X 4.81	$37/h_c$	14.87

Table 4-2: Comparison of calculated thermal resistances and experimental thermal resistances on various samples.

From the table, we can see that the thermal resistance of Sample A is indeed significantly higher than the thermal resistances of Sample C, E, F and G, which explains the experimental results in Fig. 4-10. However, based on the experimental data, when the heat flux is the lowest, the convection heat transfer coefficient between the solid and the liquid, h_c, is about 2.5 W/K·m^2, which is significantly lower than expected. The explanation for this discrepancy is due to the fact that the temperature of the vapor was assumed to be the same with the ambient temperature, 20 ^{o}C. However, a significant temperature gradient from the environment and the vapor near the liquid interface exists. The thermal resistances determined based on the experimental data actually included the convection resistance between the vapor near the liquid-vapor interface and the environment. As a result, the thermal resistances were overestimated and the h_c was underestimated. In the future, another thermocouple will be placed near the interface to estimate the temperature of the vapor in order to determine the accurate thermal resistances.

Conclusion

Thin film evaporation studies with fabricated test devices that incorporated microstructures and integrated heaters and sensors were performed. Experiments showed that within certain ranges of heat fluxes, the microstructures formed a uniform liquid layer and dissipated a reasonable heat flux with a relatively low temperature rise. Higher heat fluxes cause dry-out to occur. The critical heat flux where dry-out occurs was demonstrated to be dependent on the geometries. On pillar arrays where the liquid propagates faster, the dry-out occurs at higher heat fluxes. Moreover, the pillars act as pin fins to help dissipate heat and reduce the thermal resistance. The convection between the vapor near the liquid interface and the ambient air is also a significant part of the thermal resistance. More experiments are needed to determine the convection thermal transfer coefficient between the liquid and the solid.

Chapter 5: Future Directions

Thin film evaporation was investigated in this work and is a promising method for advanced thermal management. However, based on these initial studies, there is still significant room for improvement. In Chapter 2, the fine features on the pillars controlled the thickness of the liquid film, but the position could not be controlled. In future work, novel fabrication techniques such as multi-step lithography can be implemented to achieve local thin film control to dissipate heat for hot spots. Moreover, with the Modified Washburn's model, the propagation rate on micropillar arrays can be predicted but the accuracy of the model still needs to be improved, especially when the porosity of the pillar array is very large. Possible improvements include utilization of more accurate empirical equations or combination of empirical equation and CFD tools.

In the heat dissipation experiments where the liquid was supplied by a syringe pump and needle, the large diameter of the needle did not allow a continuous liquid stream to deposit onto the surface. In the future, smaller jet orifices will be fabricated to form continuous liquid streams to enhance the stability and repeatability of the experiments. The resistors were susceptible to scratches and damages. Possible improvements include a deposition of protection layer such as silicon dioxide or silicon nitride. In addition, the heat flux from the aluminum heaters was limited. To study the thin film evaporation at very high heat fluxes, alternative heater materials such as indium tin oxide (ITO) glasses will also be considered.

In the experiments as described in Chapter 4, the voltage applied on the heater was increased by 5 V increments, which made it difficult to find the onset point of the First Dry-out. In the future, a power supply with a GPIB interface will be programmed so that the heating power can be ramped up automatically to determine the exact location of First Dry-outs. In addition, in the design of the devices, only the conduction thermal resistance in the liquid film was considered. However, experiments show that the convection and the pin fin effect of the pillars are all important factors in the overall thermal resistance. A more detailed analysis for the thermal resistance is needed to determine the optimized microstructure geometries for thin film evaporation. Moreover, the liquid propagation in the presence of evaporation may be different from the propagation without evaporation. A comprehensive model on the transport of liquid and heat including phase change needs to be developed.

Acknowledgements

The author gratefully acknowledges the help and support of Professor Evelyn Wang, and Kuang-Han (Hank) Chu, whose ideas and guidance were instrumental in completing this work. The author would also like to acknowledge the staff and all those associated with the Microsystems Technology Laboratories at the Massachusetts Institute of Technology, who provided guidance in developing the processes and recipes to produce the devices used in this study.

Bibliography

[1] R. P. Feynman, "There's Plenty of Room at the Bottom," in *Address to the annual meeting of the American Physical Society*, California Institute of Technology, Pasadena, CA, Dec. 1959.

[2] Analog Devices. (2008, May) iMEMS Accelerometers. [Online]. HYPERLINK "http://www.analog.com/" http://www.analog.com/

[3] Fluidigm. (2008, May) Fluidigm Technology. [Online]. HYPERLINK "http://www.fluidigm.com/tech.htm" http://www.fluidigm.com/tech.htm

[4] International Roadmap Committee. (2007) The International Technology Roadmap for Semiconductors. [Online]. HYPERLINK "http://www.itrs.net/" http://www.itrs.net/

[5] J. R. Thome, "The New Frontier in Heat Transfer: Microscale and Nanoscale Technologies," *Heat Transfer Engineering*, vol. 27, no. 9, pp. 1-3, 2006.

[6] S. Krishnan, S.V.Garimella, G.M.Chrysler and R.V.Mahajan, "Towards a Thermal Moore's Law," *IEEE Transactions on Advanced Packaging*, Vol. 30, No. 3, Aug. 2007

[7] S.G.Kandlikar and A.V.Bapat, "Evaluation of Jet Impingement, Spray and Microchannel Chip Cooling Options for High heat Flux Removal", *Heat Transfer Engineering*, Vol. 28, No. 11, pp. 911-923, Nov. 2007

[8] Wikipedia (2009) Solar Cell [Online]. HYPERLINK "http://en.wikipedia.org/wiki/Solar_cell" http://en.wikipedia.org/wiki/Solar_cell

[9] A. Faghri and Z. Guo, "Challenges and opportunities for thermal management issues related to fuel cell technology and modeling", *International Journal of Heat and Mass Transfer*, Vol. 48, No. 19-20, 2005

[10] I.Mudawar, "Assessment of High-Heat-Flux Thermal Management Schemes", *IEEE Transactions on Components and Packaging Technologies*, Vol. 24, No. 2, pp.122-141, Jun. 2001.

[11] N.Zuber, "Hydrodynamic Aspects of Boiling Heat Transfer", AEC Report AECU-4439, Jun.1959

[12] V.K.Dhir and S.P.Liaw, "Framework for a Unified Model for Nucleate and Transition Pool Boiling", *ASME Journal of Heat Transfer*, Vol. 111, pp. 739-746, 1989

[13] S.G.Liter and M.Kaviany, "Pool-boiling CHF enhancement by modulated porous-layer coating: theory and experiment", *International Journal of Heat and Mass Transfer*, Vol. 44(2001), pp. 4287-4311

[14] S.J.Kim, I.C.Bang, J.Buongiorno and L.W.Hu, "Surface Wettability Cange during Pool Boiling of Nanofluids and its effect on Critical Heat Flux", *Applied Physics Letters*, Vol. 89, 2006

[15] S.M. You, J.H.Kim and K.H.Kim, "Effect of Nanoparticles on Critical Heat Flux of Water in Pool Boiling Heat Transfer", Applied Physics Letters, Vol. 83, No. 16, pp.

3374-3376, 2003

[16] R.Chen,M-C. Lu, V.Srinivasan, Z.Wang, H.H.Cho and A. Majumdar, "Nanowires for Enhanced Boiling Heat Transfer", Nano Letters, Vol. 9, No. 2, pp. 548-553, 2009

[17] A.Kosar and Y.Peles, "Thermal Hydraulic Performance of MEMS-Based Pin Fin Heat Sink", *Journal of Heat Transfer*, Vol. 128, No. 2, pp. 121-131, 2006

[18] E.N.Wang, L.Zhang, L.Jiang, J-M,Koo, J.G.Maveety, E.A.Sanchez,K.E.Goodson and T.W.Kenny, "Micromachined Jets for Liquid Impingement Cooling of VLSI Chips", *Journal of Microelectromechanical Systems*, Vol. 13, No. 5, Oct 2004

[19] L.Lin and R.Ponnappan, "Heat Transfer Characteristics of Spray Cooling in a Closed Loop", *International Journal of Heat and Mass Transfer*, Vol. 46, No. 20, pp. 3737-3746, 2003

[20] C.E.Bash, C.D.Patel and R.K.Sharma, "Inkjet Assisted Spray Cooling of Electronics", *2003 International Electronic Packaging Technical Conference and Exhibition, July 6-11, 2003*, Vol. 2, pp. 119-127, 2003

[21] J.H.Kim,Sm.M.You and S.U.S.Choi, "Evaporative Spray Cooling of Plain and Microporous Coated Surfaces", *International Journal of Heat and Mass Transfer*, Vol. 47, No. 14-16, pp. 3307-3315, 2004.

[22] E.A.Silk,J.Kim and K.Kiger, "Investigation of Enhanced Surface Spray Cooling", *2004 ASME International Mechanical Engineering Congress and Exposition, IMECE, Novermber 13-19, 2004*, Vol. 375, pp. 685-690, 2004

[23] J.S.Coursey, J.Kim and K.T.Kger, "Spray Cooling of Small Pitched, Straight-Finned, Copper Heat Sink", *2005 ASME International Mechanical Engineering Congress and Exposition, IMECE, November 5-11, 2005,* Vol. 376 HTD, pp. 271-277, 2005

[24] D.D.Hall and I.Mudawar, "Experimental and Numerical Study of Quenching Complex-shaped Metallic Alloys with Multiple, Overlapping Sprays", *International Journal of Heat and Mass Transfer*, Vol. 38, pp. 1201-1216, 1995

[25] M. Ohadi, J.Qi, and J. Lawler, "Ultra-thin Film Evaporation (UTF) Application to Emerging Technologies in Cooling of Microelectronics", *Microscale Heat Transfer Fundamentals and Applications*, Vol. 193, pp. 321-338, 2006

[26] R. N. Wenzel, "Resistance of Solid Surfaces to Wetting by Water", *Industrial and Engineering Chemistry*, Vol. 28(8), pp. 988-994, 1936

[27] A. B. D. Cassie and S. Baxter, "Wettability of Porous Surfaces", *Transactions of the Faraday Society*, Vol. 40, pp. 546-551, 1944

[28] Z. Yoshimitsu, A. Nakajima, T. Watanabe and K. Hashimoto, "Effects of Surface Structure on the Hydrophobicity and Sliding Behavior of Water Droplets", *Langmuir*, Vol. 18(15), pp. 5818-5822, 2002

[29] N. A. Patankar, "Mimicking the Lotus Effect: Influence of Double Roughness Structures and Slender Pillars", *Langmuir*, Vol. 20(19), pp. 8209-8213, 2004

[30] J. Jopp, H. Grull and R. Yerushalmi-Rozen, "Wetting Behavior of Water Droplets on Hydrophobic Microtextures of Comparable Size", *Langmuir*, Vol. 20(23), pp. 10015-

10019, 2004

[31] R. Furster, W. Barthlott, C. Neinhuis and P. Walzel, "Wetting and Self-cleaning properties of Artificial Superhydrophobic Surfaces", *Langmuir*, Vol. 21(3), pp. 956-961, 2005

[32] W. Li and A. Amirfazli, "Microtextured Superhydrophobic Surfaces: A Thermodynamic Analysis", *Advances in Colloid and Interface Science*, Vol. 132(2), p. 51, 2007

[33] A. Tuteja, W. Choi, M. L. Ma, J. M. Marbry, S. A. Mazzella, G. C. Rutledge, G. H. McKinley and R. E. Cohen, "Designing Superoleophobic Surfaces", *Science*, Vol. 318(5856), pp. 1618-1622, 2007

[34] A. Ahuja, J. A. Taylor, V. Lifton, A. A. Sidorenko, T. R. Salamon, E. J. Lobaton, P. Kolodner and T. N. Krupenkin, "Nanonails: A Simple Geometrical Approach to Electrically Tunable Superlyophobic Surfaces", *Langmuir*, Vol. 24(1), pp. 9-14, 2008

[35] F. C. Cebeci, Z. Z. Wu, L. Zhai, R. E. Cohen and M. F. Rubner, "Nanoporosity-driven Superhydrophilicity: A Means to Create Multifunctional Antifogging Coatings", *Langmuir*, Vol. 22(6), pp. 2856-2862, 2006

[36] C. W. Extrand, S. I. Moon, P. Hall and D. Schmidt, "Superwetting of Structured Surfaces", *Langmuir*, Vol. 23(17), pp. 8882-8890, 2007

[37] L. Courbin, E. Denieul, E. Dressaire, M. Roper, A. Ajdari and H. A. Stone, "Imbibition by Polygonal Spreading on Microdecorated Surfaces", *Nature Materials*, Vol. 6(9), pp. 661-664, 2007

[38] M. Sbragaglia, A. M. Peters, C. Pirat, B. M. Borkent, R. G. Lammertink, M. Wessling and D. Lohse, "Spontaneous Breakdown of Superhydrophobicity", *Physics Review Letters*, Vol. 99(15), 2007

[39] C. Pirat, M. Sbragaglia, A. M. Peters, B. M. Borkent, R. G. Lammertink, M. Wessling and D. Lohse, "Multiple Time Scale Dynamics in the Breakdown of Superhydrophobicity", *Europhysics Letters*, Vol. 81(6), 2008

[40] E. W. Washburn, "The Dynamics of Capillary Flow", *Physics Review*, Vol. 17(3), pp. 273-283, 1921

[41] A. Faghri, "Heat Pipe Science and Technology", Washington, DC: Taylor & Francis, 1995

[42] R. A. Serway, "Principles of Physics (2nd ed.)", Fort Worth, Texas; London: Saunders College Pub., 1998

Appendix A

The derivation of the Equation (2-1):

As shown in Fig. 2-5(d), when a volume of liquid ΔV is supplied from the droplet, the liquid film can either propagate in separated layers or in a uniform thickness. The changes in surface energy are defined as ΔE_1 and ΔE_2, respectively. When the liquid propagates beneath the edge of height h_l, the increase in area of the liquid-vapor interface is given by

$$\Delta S_{LV} = \frac{\Delta V}{h_l}.$$

The area of solid surface covered by liquid becomes

$$\Delta S_{SL} = (1 + \frac{\pi d_l h_l}{1 - \frac{\pi d_l^2}{4l^2}})\frac{\Delta V}{h_l},$$

where d_l is the diameter of the pillar below the edge and l is the center-to-center distance between neighboring pillars. Therefore, the change in surface energy when the liquid is only beneath the edge is given by

$$\Delta E_1 = \frac{\Delta V}{h_l}\gamma_{LV} + \frac{\Delta V}{h_l}(1 + \frac{\pi d_l h_l}{l^2 - \frac{\pi d_l^2}{4}})(\gamma_{SL} - \gamma_{SV}),$$

where the surface energies associated with the liquid-air, air-solid, and solid-liquid interface are denoted as γ_{LV}, γ_{SV}, and γ_{SL}, respectively. If the parameters A, B and C are defined as

$$A=\frac{d_l}{l}, B=\frac{d_u}{d_l}, C=\frac{h_l}{h_u+h_l}, \text{ then}$$

$$\begin{aligned}\Delta E_1 &= \frac{\Delta V}{h_l}\gamma_{LV}+\frac{\Delta V}{h_l}[1+\frac{\pi d_l C(h_u+h_l)}{l^2-\frac{\pi d_l^2}{4}}](\gamma_{SL}-\gamma_{SV})\\ &= \frac{\Delta V}{C(h_u+h_l)}\gamma_{LV}+\frac{\Delta V}{h_l}[1+\frac{\pi d_l C(h_u+h_l)}{l^2-\frac{\pi d_l^2}{4}}](\gamma_{SL}-\gamma_{SV})\\ &= \frac{\Delta V}{C(h_u+h_l)}\gamma_{LV}+\frac{\Delta V}{C(h_u+h_l)}[1+\frac{\pi d_l C(h_u+h_l)}{l^2-\frac{\pi d_l^2}{4}}](\gamma_{SL}-\gamma_{SV}),\end{aligned}$$

where h_u is the upper pillar height and d_u is the upper pillar diameter.

Similarly, by calculating the change in the liquid-air interface and the solid area covered by the liquid when the liquid fills the entire pillar, the change in surface energy is given by

$$\Delta E_2 = \frac{\Delta V(l^2-\frac{\pi d_u^2}{4})}{(l^2-\frac{\pi d_u^2}{4})h_u+(l^2-\frac{\pi d_l^2}{4})h_l}\gamma_{LV}+\frac{\Delta V(l^2-\frac{\pi d_u^2}{4}+\pi d_l h_l+\pi d_u h_u)}{(l^2-\frac{\pi d_u^2}{4})h_u+(l^2-\frac{\pi d_l^2}{4})h_l}(\gamma_{SL}-\gamma_{SV}).$$

Given the same definitions for parameters *A*, *B*, and *C*,

$$\Delta E_2 = \frac{\Delta V(1-\frac{\pi A^2B^2}{4})}{(1-\frac{\pi A^2B^2}{4})(1-C)(h_u+h_l)+(1-\frac{\pi A^2}{4})C(h_u+h_l)}\gamma_{LV} + \frac{\Delta V[l-\frac{\pi A^2B^2 l}{4}+\pi AC(h_u+h_l)+\pi AB(1-C)(h_u+h_l)]}{(l-\frac{\pi A^2B^2 l}{4})(1-C)(h_u+h_l)+(l-\frac{\pi A^2 l}{4})C(h_u+h_l)}(\gamma_{SL}-\gamma_{SV}).$$

Therefore, $\frac{\Delta E_1}{\Delta V}-\frac{\Delta E_2}{\Delta V}$, which corresponds to the difference of the normalized energy between state (ii) and state (iv) in Fig. 2 can be calculated as:

$$S \equiv \frac{\Delta E_1}{\Delta V} - \frac{\Delta E_2}{\Delta V} = \gamma_{LV}\frac{1}{h_u+h_l}(\frac{1-\frac{\pi A^2B^2}{4}}{(1-\frac{\pi A^2B^2}{4})(1-C)+(1-\frac{\pi A^2}{4})C} - \frac{1}{C})$$

$$+(\gamma_{SL}-\gamma_{SV})\frac{1}{h_u+h_l}(\frac{l-\frac{\pi A^2B^2l}{4}+\pi ACh+\pi AB(1-C)(h_u+h_l)}{(l-\frac{\pi A^2B^2l}{4})(1-C)+(l-\frac{\pi A^2l}{4})C} - \frac{l-\frac{\pi A^2l}{4}+\pi AC(h_u+h_l)}{C(l-\frac{\pi A^2l}{4})})$$

$$=\gamma_{LV}\frac{1}{h_u+h_l}(\frac{1}{(1-C)+\frac{(1-\frac{\pi A^2}{4})}{(1-\frac{\pi A^2B^2}{4})}C} - \frac{1}{C}) + (\gamma_{SL}-\gamma_{SV})\frac{1}{h_u+h_l}(\frac{1-\frac{\pi A^2B^2}{4}}{(1-\frac{\pi A^2B^2}{4})(1-C)+(1-\frac{\pi A^2}{4})C})$$

$$+\frac{\pi A(h_u+h_l)(C+B(1-C))}{(l-\frac{\pi A^2B^2l}{4})(1-C)+(l-\frac{\pi A^2l}{4})C} - \frac{1}{C} - \frac{\pi A(h_u+h_l)}{l-\frac{\pi A^2l}{4}})$$

$$\therefore S = \gamma_{LV}\frac{1}{h_u+h_l}(\frac{1}{\Lambda_1}-\frac{1}{C})$$

$$-\gamma_{LV}\frac{1}{h_u+h_l}\cos\theta(\frac{1}{\Lambda_1}-\frac{1}{C}) - \gamma_{LV}\frac{1}{l}\cos\theta(\frac{\pi A(C+B(1-C))}{\Lambda_2} - \frac{\pi A}{1-\frac{\pi A^2}{4}})$$

where: $\Lambda_1 = (1-C)+\frac{(1-\frac{\pi A^2}{4})}{(1-\frac{\pi A^2B^2}{4})}C, \quad \Lambda_2 = (1-\frac{\pi A^2B^2}{4})(1-C)+(1-\frac{\pi A^2}{4})C.$

Appendix B

DRIE Recipe for the Fabrication of Pillars with a Single Notch

Recipe 1

	Etch	Passivation
Time(s)	7.0	5.5
C_4F_8 Flow Rate (sccm)	0	40±25%
SF_6 Flow Rate (sccm)	105±25%	0±5%
Pressure (mT)	32	14
Platen RF Power (W)	120	60
Coil RF Power (W)	800	600

Recipe 2

	Etch	Passivation
Time(s)	21.0	18.0
C_4F_8 Flow Rate (sccm)	0±25%	95±25%
SF_6 Flow Rate (sccm)	140±25%	0±25%
Pressure (mT)	94	31
Platen RF Power (W)	140	0
Coil RF Power (W)	600	600

To fabricate pillars with *C*=0.49, Recipe 1 was used for 4 minutes then Recipe 2 was used for 39.0 seconds (one cycle), and Recipe 1 was used for another 3 minutes.

To fabricate pillars with *C*=0.63, Recipe 1 was used for 2 minutes then Recipe 2 was used for 39.0 seconds (one cycle), and Recipe 1 was used for another 5 minutes.

Appendix C

MATLAB code to calculate the propagation rate with the modified Washburn's Model:

```
h=; %Input height of the pillars%
d=; %Input diameter of the pillars%
la=; %Input spacing between the pillars%
gammaLV=0.072; %Surface Tension of the liquid%
theta=38/180*pi; %Contact angle of the lquid on the solid%
miu=1e-3;%Viscosity of teh liquid%
Pv=0;
l=d+la; %Period of the array%
Q=1/l*h*(l^2-pi*d^2/4); %Flow rate when the propagation velocity is
1m/s%
for i=1e-8:1e-8:d/2
    W=l-sqrt(d^2/4-(d/2-i)^2)*2;
    al=W/h;
    fRe=24*(1-1.3553*al+1.9467*al^2-1.7012*al^3+0.9564*al^4-
0.2537*al^5);
    Dh=4*h*W/(2*h+W);
    KP=Dh^2*(W/l)/2/(fRe);
    dP=miu*Q/(h*W)*1e-8/KP;
    Pv=Pv+dP;
end
Pd(m,n)=Pv*2+Q/l/h^3*3*miu*(l-d);%Pressure drop across one pillar%
k(m,n)=2*(0.072*(l^2-0.25*pi*d^2)*(cos(theta)-
1)+0.072*cos(theta)*pi*d*h)/Pd(m,n)/l/h;
```

Appendix D

The fabrication process of the testing chips with microstructures on the front side and resistors on the back side.

Starting Substrate
Processing will be performed on: Si wafer (thickness: 500um)

Step	Description
1. Silicon Dioxide Growth	Grow an oxide layer of about 100nm
2. RIE	Etch away silicon dioxide on the front side
3. Photolithography	PR Coating: Use AZ4630 as positive PR Soft bake: Oven bake wafer UV exposure: exposure using mask for electrode pattern Develop: Develop PR Hard bake: Oven bake wafer
4. Deep RIE	Etch 20um micro pillar with sts machine.
5. Photolithography (backside)	PR Coating: Use AZ5214E as negative PR Pre bake UV exposure: exposure using mask for heaters Post Bake Flood exposure Develop: Develop PR in AZ422
6. Ebeam evaporation	Deposit 300 nm Aluminum.
7. Lift-off	Acetone Lift-off

8. Rinse and clean	Clean the wafer with Methanol and IPA
9. Photolithography (backside)	PR Coating: Use AZ5214E as negative PR Pre bake UV exposure: exposure using mask for heaters Post Bake Flood exposure Develop: Develop PR in AZ422
10. Ebeam evaporation	Deposit 200 nm Aluminum.
11. Lift-off	Acetone Lift-off
12. Rinse and clean	Clean the wafer with Methanol and IPA
13. Dicing	Dice chips with dice-saw

Appendix E

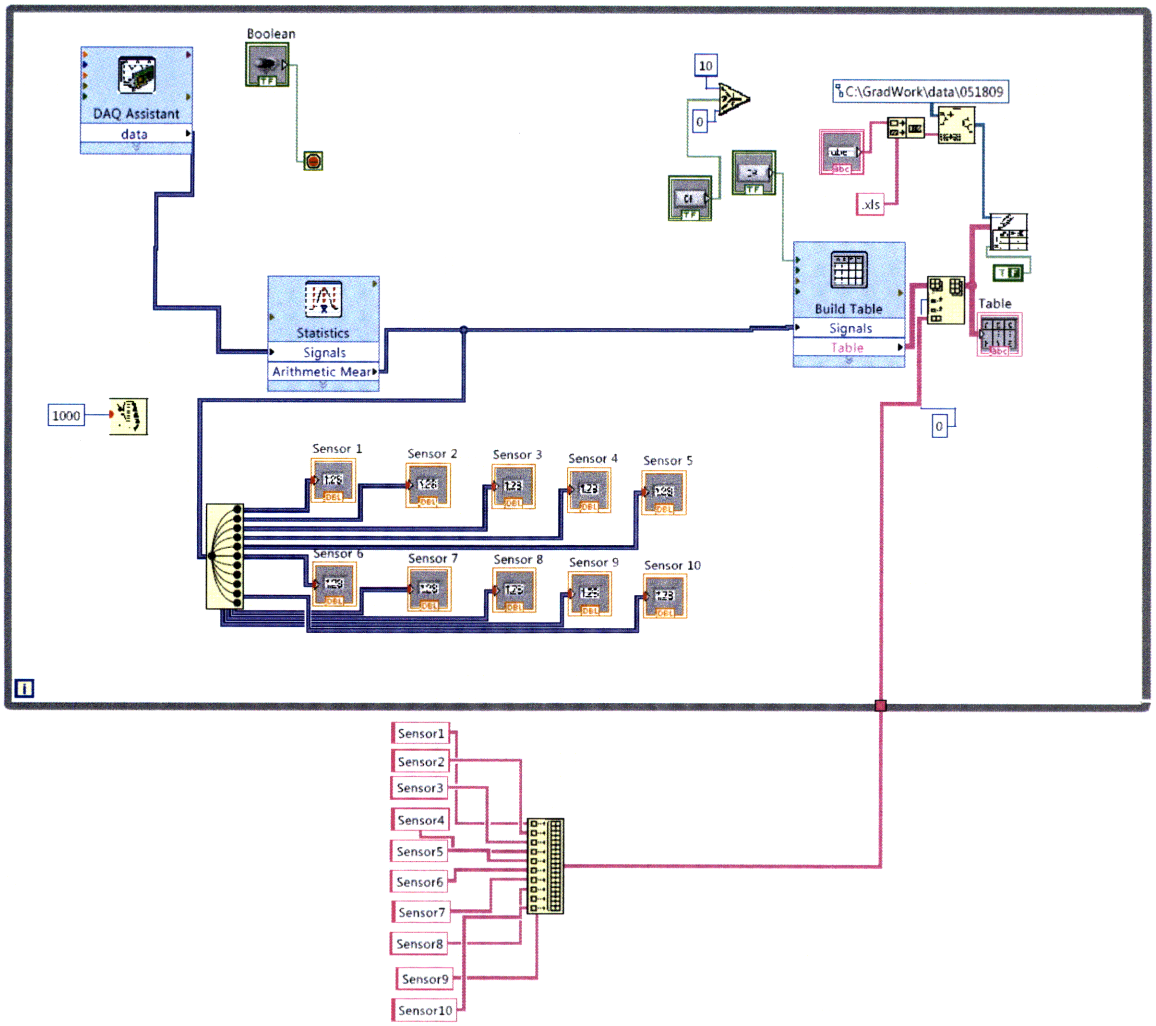

Fig.E-1: Schematic Layout of the LabView program used to capture data. The data flows from left to right in the schematic.

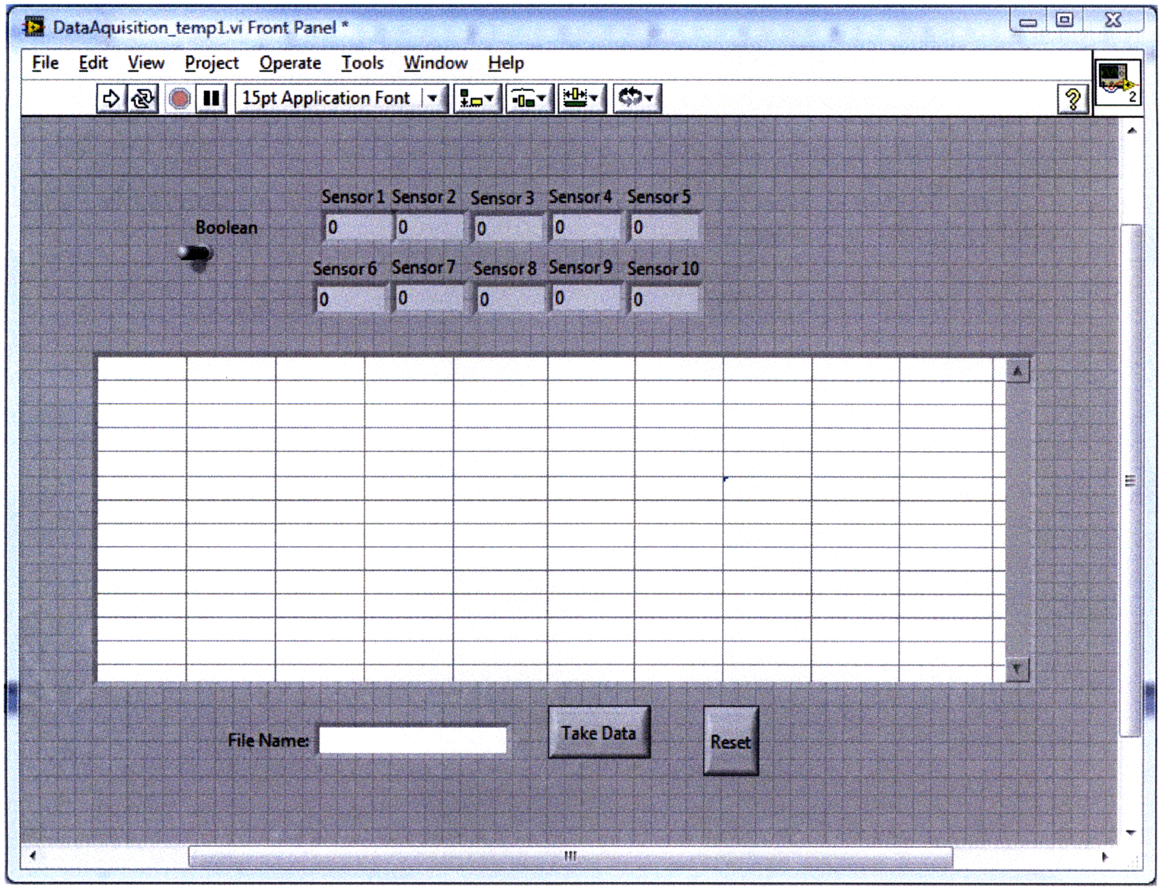

15pt Application Font

Sensor 1	Sensor 2	Sensor 3	Sensor 4	Sensor 5
0	0	0	0	0

Sensor 6	Sensor 7	Sensor 8	Sensor 9	Sensor 10
0	0	0	0	0

File Name:

Fig.E-2: Interface diagram for the LabView program used to capture data. Data was recorded automatically when the program was started